ROYAL SOCIETY
OF CHEMISTRY

## PAPER

Check for updates

# Experimental and theoretical study of β-As₂Te₃ under hydrostatic pressure†‡

R. Vilaplana, [iD] *[a] S. Gallego-Parra, [iD] [b] E. Lora da Silva, [iD] [c] D. Martínez-García,[d]
G. Delaizir,[e] A. Muñoz, [iD] [f] P. Rodríguez-Hernández, [iD] [f] V. P. Cuenca-Gotor, [iD] [b]
J. A. Sans,[b] C. Popescu, [iD] [g] A. Piarristeguy[h] and F. J. Manjón [iD] [b]

We report a joint experimental and theoretical high-pressure study of the structural and vibrational properties of tetradymite-like (R3̄m) β-As₂Te₃. Two samples have been characterized by angle-dispersive synchrotron powder X-ray diffraction and Raman scattering measurements under hydrostatic conditions with the help of *ab initio* calculations. One sample was synthesized at high pressure and high-temperature conditions with a Paris-Edinburg cell and the other by the melt-quenching technique. Both β-As₂Te₃ samples show the same properties and exhibit two isostructural phase transitions of order higher than 2, *i.e.* of electronic origin, near 2.0(2) and 6.0(5) GPa that are compatible with the changes predicted by recent electronic band structure calculations. The first isostructural phase transition can be attributed to the topological quantum phase transition from a trivial insulator to a topological insulator, passing through a 3D Dirac topological semimetal. This topological transition, specific to β-As₂Te₃, is not observed in isostructural Te-based sesquichalcogenides α-Sb₂Te₃ and α-Bi₂Te₃ that are topological insulators at room conditions. The second isostructural phase transition is likely related to an insulator-metal transition. Additionally, we have observed two partially reversible first-order phase transitions in β-As₂Te₃ above 10 and 17 GPa. We have found a high anharmonic behavior of the two Raman-active modes with the lowest frequencies in β-As₂Te₃ that explains the already reported ultra-low lattice thermal conductivity of β-As₂Te₃. Moreover, we have studied the similarities of β-As₂Te₃ with α-Sb₂Te₃ and α-Bi₂Te₃ (two of the best thermoelectric materials), thus providing insights into the origin of the ultra-low lattice thermal conductivity values in these compounds related to unconventional chemical bonds present in these isostructural materials.

## 1. Introduction

The most efficient thermoelectric (TE) materials for room temperature applications are based on Bi₂Se₃, Sb₂Te₃, and Bi₂Te₃ sesquichalcogenides that usually crystallize in a rhombohedral structure (space group (SG) R3̄m, No. 166) typical of mineral tetradymite (Bi₂Te₃).[1–4] Therefore, there is a strong interest in studying all tetradymite-type B₂X₃ sesquichalcogenides,

[a] *Centro de Tecnologías Físicas: Acústica, Materiales y Astrofísica, MALTA Consolider Team, Universitat Politècnica de València, 46022 Valencia, Spain.*
 *E-mail: rovilap@fis.upv.es*
[b] *Instituto de Diseño para la Fabricación y Producción Automatizada, MALTA Consolider Team, Universitat Politècnica de València, 46022 Valencia, Spain*
[c] *Institute of Physics for Advanced Materials, Nanotechnology and Photonics, Department of Physics and Astronomy, Faculty of Sciences, University of Porto, 4169-007 Porto, Portugal*
[d] *Departamento de Física Aplicada – ICMUV, MALTA Consolider Team, Universitat de València, Burjassot, Spain*
[e] *Institut de Recherche sur les Céramiques (IRCER), UMR CNRS 7315, Centre Européen de la Céramique, 87068 Limoges, France*
[f] *Departamento de Física, Instituto de Materiales y Nanotecnología, MALTA Consolider Team, Universidad de La Laguna, Tenerife, Spain*
[g] *ALBA-CELLS, Cerdanyola, E-08290 Barcelona, Spain*
[h] *ICGM, Univ Montpellier, CNRS, ENSCM, Montpellier, France*

† PACS: 31.15.A-, 61.05.cp, 62.50.-p, 64.30.Jk, 71.15.Mb

‡ Electronic supplementary information (ESI) available: Rietveld refinements of sample #2 at ambient pressure; experimental HP-XRD patterns of sample #2 at selected pressures; Rietveld refinements similar pressure of sample #1 and #2; sequences of experimental HP-XRD patterns of sample #1 and #2; relaxed XRD pattern of sample #1; comparative of experimental XRD patterns of β-As₂Te₃ and α-As₂Te₃ at about 17.6 GPa; theoretical (PBE + D3) axial compressibilities and bulk modulus for isostructural β-As₂Te₃, α-Sb₂Te₃, and α-Bi₂Te₃ *vs.* pressure; theoretical (PBE + D3) interlayer and intralayer distances for isostructural β-As₂Te₃, α-Sb₂Te₃ and α-Bi₂Te₃ *vs.* pressure; theortical bond angle variance, quadratic elongation, and effective coordination number of some octahedrons; bader charges in β-As₂Te₃ including SOC; theoretical (PBE + D3) dielectric constants and average born effective charges of As and Te atoms; schematic view of the crystalline structure of α-As₂Te₃ of As₂Te₃ with β-Bi₂Te₃ at about 14 GPa. See DOI: https://doi.org/10.1039/d2tc03357g

This journal is © The Royal Society of Chemistry 2023

*J. Mater. Chem. C*, 2023, **11**, 1037–1055 | **1037**

especially those of group-15 elements (As, Sb, Bi). Further interest in these materials aroused since $Bi_2Se_3$, $Sb_2Te_3$, and $Bi_2Te_3$ were discovered to be 3D topological insulators (TIs), with important theoretical and technological implications, including the discovery of exotic fermions and the implementation of devices for spintronics and quantum computation.[5–7] Whereas the properties of tetradymites $Bi_2Se_3$, $Sb_2Te_3$, and $Bi_2Te_3$ have been considerably explored in the last decade, much less attention has been paid to the isostructural compound $\beta$-$As_2Te_3$,[8] which is one of the two polymorphs of $As_2Te_3$ known at ambient conditions. It is known that the stable phase of $As_2Te_3$ at ambient conditions is $\alpha$-$As_2Te_3$ which crystallizes in the monoclinic (SG $C2/m$, No. 12).[9] Therefore, it would be very interesting to improve TE or TI properties to explore the properties of $\beta$-$As_2Te_3$ since alloying of $Bi_2Te_3$, $Sb_2Te_3$, and $Bi_2Se_3$ with $\beta$-$As_2Te_3$ has been barely explored.[10]

$\beta$-$As_2Te_3$ was first obtained from $\alpha$-$As_2Te_3$ at high pressure (HP), and high-temperature (HT) conditions[11] and afterwards by quenching from a melted $As_2Te_3$ sample.[8,12,13] $\beta$-$As_2Te_3$ is a metastable phase at room conditions that transforms irreversibly into the $\alpha$ phase above 480 K at room pressure and also transforms into another polymorph with SG $P2_1/m$ ($\beta'$-$As_2Te_3$) below 210 K.[14] Interestingly, the thermoelectric properties of $\beta$-$As_2Te_3$ were found to be better than $\alpha$-$As_2Te_3$ upon Sn and Bi doping.[15–19] Moreover, a notable increase of the thermoelectric power was found in $\alpha$-$As_2Te_3$ at HP under non-hydrostatic conditions, which was followed by a pressure-induced structural phase transition (PT) that was assumed to be from the $\alpha$ to the $\beta$ phase near 7.0 GPa.[20] This PT was not confirmed in subsequent HP studies of the $\alpha$ phase under more hydrostatic conditions.[21–23]

Despite very interesting properties have been predicted in several theoretical studies of the $\beta$ phase even at HP,[24–29] no experimental HP study of the $\beta$ phase has been conducted yet, to our knowledge. Experimental HP studies have only explored the behavior of the $\alpha$ phase and glassy $As_2Te_3$.[30–33] Among theoretical studies of $\beta$-$As_2Te_3$, a figure of merit ($ZT$) of 0.7 has been predicted for $\beta$-$As_2Te_3$,[25] which is of the order of the $ZT$ values of the well-known thermoelectric material $\alpha$-$Bi_2Te_3$.[4] In the same context, a very small lattice thermal conductivity, $\kappa_L$, has been predicted for $\beta$-$As_2Te_3$,[27,29] which has been experimentally confirmed.[15,17] For these calculations, the electronic band structure of $\beta$-$As_2Te_3$ has been thoroughly studied, and spin–orbit coupling (SOC) has been found to be an essential requirement to obtain a good theoretical description of the electronic band structure as well as of the TE and TI properties. In particular, according to the most recent and accurate calculations,[29] $\beta$-$As_2Te_3$ is predicted to be a trivial insulator with a very narrow (0.3 eV) indirect bandgap near the $Z$ point. Calculations have shown that $\beta$-$As_2Te_3$ undergoes a topological quantum phase transition (TQPT) under uniaxial strain near 1.7 GP[28] and under hydrostatic pressure near 2 GPa due to the closing of the direct bandgap at the $\Gamma$ point.[29] Around 2 GPa, $\beta$-$As_2Te_3$ becomes a 3D topological Dirac semimetal with a single Dirac cone in its electronic structure at the $\Gamma$ point. Above 2 GPa, the bandgap reopens, and $\beta$-$As_2Te_3$ becomes a 3D
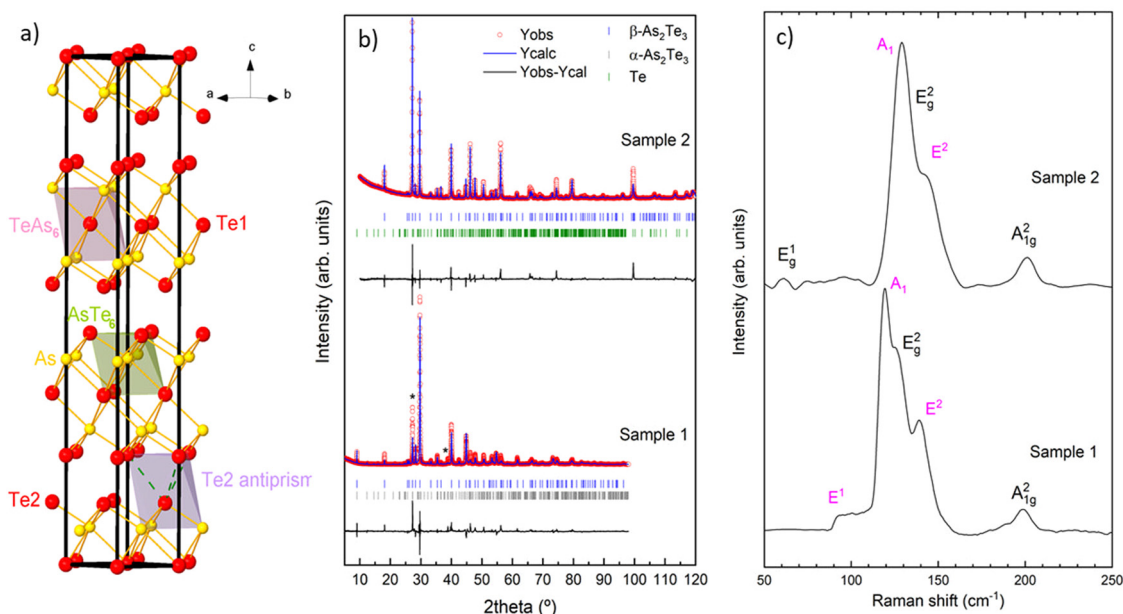
TI, as isostructural $Bi_2Se_3$, $Sb_2Te_3$, and $Bi_2Te_3$.[29] The different behavior of $\beta$-$As_2Te_3$ is due to its smaller SOC, so uniaxial stress or hydrostatic pressure is needed to transform this compound from a trivial insulator to a TI by helping to decrease the bandgap and allow SOC to induce a band inversion.[28,29]

The tetradymite crystal structure of $\beta$-$As_2Te_3$ is usually described with a hexagonal unit cell that contains three quintuple layer (QL) atomic blocks (Te2–As–Te1–As–Te2). In this structure, As atoms are octahedrally coordinated, forming a distorted octahedron (hereinafter $AsTe_6$) (see Fig. 1). In the $AsTe_6$ distorted octahedron, the As–Te1–Te1–Te2–Te2 central square is nonplanar and the Te2–As and As–Te1 axial bonds that complete the octahedron are neither collinear nor strictly perpendicular to the central square. In addition to this classical picture of the tetradymite structure,[34,35] we will show that it is helpful to consider two additional octahedra in the tetradymite structure of $\beta$-$As_2Te_3$. One is a distorted octahedron associated with the Te1 atom at the center of QL (hereinafter $TeAs_6$), with its axis As–Te1–As being non-perpendicular to the square plane formed by Te1–As–As–As–As (see Fig. 1) and the other is a highly distorted octahedron (see Fig. 1) associated with the Te2 atom (hereinafter named antiprism). This latter octahedron forms an antiprism, as introduced by Morin et al.[14] because the Te2 atom is linked to three short bonds to three As atoms inside the QL and three long distances to Te2 atoms of the neighbour QL.

Tetradymite-like QLs have been considered to be linked by van der Waals (vdW) interactions along the hexagonal $c$ axis and show a mixture of ionic-covalent interatomic bonds inside the QLs. However, this traditional vision has been questioned in recent years. AX, $B_2X_3$, and $AB_2X_4$ chalcogenides with tetradymite structure, with $A$ and $B$ being group-14 (Ge, Sn, Pb) and group-15 (As, Sb, Bi) cations, respectively, have been suggested to exhibit an unconventional type of bonding, named as resonant bonding, metavalent bonding, and hypervalent bonding, that has been recently considered to be a case of the multicenter bonding. This unconventional type of bonding in solids has been considered responsible for the exotic properties of these materials, including phase change materials for computer memories, topological properties, as well as high thermoelectric and photovoltaic efficiencies.[36–50]

In this context, it must be mentioned that some interesting reviews[1,2] of tetradymite sesquichalcogenides and topological materials have put the focus on the link between chemical bonding and low lattice thermal conductivity and the highly-efficient TE and TI properties.[3,4,50] Consequently, it is very interesting to characterize the properties of tetradymite $\beta$-$As_2Te_3$ at HP and to compare them with those of isostructural (Sb, Bi)$_2Te_3$ to shed light on the TE and TI properties of tetradymite sesquichalcogenides.

In this work, we report a joint experimental and theoretical HP study of the structural and vibrational properties of tetradymite $\beta$-$As_2Te_3$ to explore its properties under compression and check its pressure-induced PTs, including isostructural phase transitions (IPT) or possible electronic topological transition (ETT) as found in isostructural group-15 $B_2X_3$ sesquichalcogenides.

**1038** | *J. Mater. Chem. C*, 2023, **11**, 1037–1055

This journal is © The Royal Society of Chemistry 2023

**Fig. 1** (left) Hexagonal unit cell of the tetradymite-like structure of β-As$_2$Te$_3$. Note the three different distorted octahedra associated with the Te1 atom (TeAs$_6$, top), the As atom (AsTe$_6$, center), and to Te2 atom (antiprism, bottom). (center) Powder XRD patterns of samples 1 (down) and 2 (top) at room conditions. Rietveld refinement and Le Bail analysis of the experimental XRD patterns of sample 1 and sample 2, respectively, and the corresponding residuals are shown. Asterisks in sample 1 indicate the peaks associated with Te impurity. (left) At room conditions, RS spectra of samples 1 (down) and 2 (top). Peaks related to β-As$_2$Te$_3$ (black colour) and trigonal Te (magenta colour) are indicated.

For this purpose, we have studied two different β-As$_2$Te$_3$ samples: (i) a sample synthesized at HP and HT by using a Paris-Edinburgh cell (hereinafter sample #1) and (ii) a sample synthesized by the melt-quenching technique (hereinafter sample #2). Both samples have been characterized by X-ray diffraction (XRD) and Raman scattering (RS) measurements at room pressure (RP) and at HP, and the results have been nicely compared with *ab initio* calculations.

We will show that both β-As$_2$Te$_3$ samples show the same properties and exhibit two IPTs of order higher than 2 near 2 and 6 GPa that are compatible with the changes predicted by recent electronic band structure calculations.[29] Moreover, we will show that β-As$_2$Te$_3$ undergoes two partially reversible first-order PTs around 10 and 17 GPa. We will show that analyzing the polyhedral distortions of the tetradymite phase gives information on the IPTs. Finally, we provide a comparison of both the structural and vibrational properties of β-As$_2$Te$_3$ with its isostructural compounds α-Bi$_2$Se$_3$, α-Sb$_2$Te$_3$, and α-Bi$_2$Te$_3$ and comment on the theoretical ultralow lattice thermal conductivity of β-As$_2$Te$_3$ and its relation to the anharmonicity to improve the good thermoelectric character of tetradymites.

## 2. Synthesis of the samples

All measurements have been performed on two samples of β-As$_2$Te$_3$. Sample #1 was synthesized at HP (3–4 GPa) and HT (633–783 K) conditions using a Paris-Edinburgh press equipped with two opposed conical tungsten-carbide anvils, as suggested in ref. 11. Boron nitride acted as the pressure-transmitting medium for a compacted polycrystalline powder sample of commercial α-As$_2$Te$_3$ (Alfa-Aesar, purity 99.999%). An outer small graphite tube containing the boron nitride cylinder was used as a heating element. Two molybdenum discs, placed on the bases of the graphite oven, acted as electrodes for the heating system. The sample assembly was introduced into a fired pyrophyllite gasket (treated previously at 1223 K for 1 hour and 30 min). A Teflon ring was added around the pyrophyllite gasket to limit the lateral extrusion during compression and to increase the pressure-load efficiency. The oil pressure in the ram was raised by using a simple hand-operated hydraulic pump. The sample was heated by driving a DC current across the graphite furnace, using a computer-controlled power supply. Pressure and temperature were determined by load-applied and power-temperature calibration curves with experimental error estimated to be less than 5%. The pressure upstroke was performed in two steps with a 2 min plateau at 1.5(2) GPa. After reaching the target pressure, the temperature was increased linearly from RT to the final temperature for 10 min and then kept at the maximum value for times ranging from 10 to 360 min. A rapid thermal quench was performed afterward. Finally, the pressure was released in a few hours, and the sample was then recovered to ambient conditions. The best β-As$_2$Te$_3$ sample was obtained at a pressure of 3 GPa and a temperature of 683 K for a synthesis time of 90 minutes. On the other hand, sample #2 was prepared from a melt with a mixture of As and Te chips weighed in stoichiometric proportion. This mixture was placed in a silica ampoule (internal diameter 6 mm) under a secondary vacuum ($< 5 \times 10^{-7}$ bar) and melted at 923 K for two hours, then quenched in a water-ice-salt

mixture bath. Sample #2 is from the same batch as the one used in the previous HT study.[14]

# 3. Experimental details of HP measurements

The characterization of both samples under compression was carried out by powder angle-dispersive HP-XRD measurements at room temperature performed at the BL04-MSPD beamline of the ALBA synchrotron facility.[51] This beamline is equipped with Kirkpatrick–Baez mirrors to focus the monochromatic beam and a Rayonix CCD detector with a 165 mm diameter-active area. HP-XRD measurements were conducted up to 17.9 GPa (18.1 GPa) with X-ray wavelengths of 0.4246 Å (0.4642 Å) in sample #1 (sample #2). Both samples were loaded with a 16 : 3 : 1 methanol–ethanol–water mixture in a membrane-type diamond anvil cell (DAC), and the pressure was determined with the equation of state (EoS) of copper.[52] Integration of 2D diffraction images was performed with Dioptas software,[53] while structural analysis was carried out by Rietveld refinements and Le Bail analysis using GSAS[54] and PowderCell[55] program packages.

Vibrational characterization under pressure of both samples at room temperature was carried out by RS measurements performed with a Horiba Jobin Yvon LabRAM HR UV microspectrometer, equipped with a thermoelectrically cooled multichannel charge-coupled device detector and a 1200 grooves per mm grating that allows a spectral resolution better than 3 cm$^{-1}$. The Raman signal was collected in backscattering geometry and was excited with a 532 nm laser with a power of less than 10 mW. Phonons were analysed by fitting Raman peaks with a Voigt profile where the spectrometer resolution is taken as the fixed Gaussian width. Samples were loaded with a 16 : 3 : 1 methanol–ethanol–water mixture in a membrane-type DAC, and pressure was determined by the ruby luminescence method.[56] The shape and separation of the $R_1$ and $R_2$ ruby lines were checked at each pressure. During Raman experiments, the samples were checked to be sure that no heating effects occurred during the measurements by the incoming laser excitation.

# 4. Calculations

*Ab initio* total-energy calculations for β-As$_2$Te$_3$ were carried out within the framework of density functional theory (DFT).[57] The Vienna *Ab initio* Simulation Package (VASP)[58] was used to perform calculations with the projector augmented wave (PAW) scheme, including 6 ($5s^2 5p^4$) and 15 ($3d^{10} 4s^2 4p^3$) valence electrons for Te and As, respectively. Due to the hardness of the Te pseudopotential, the set of plane waves was extended up to a kinetic energy cutoff of 300 eV, providing highly converged results. The exchange–correlation energy was obtained in the generalized gradient approximation (GGA) with the PBEsol prescription[59] as well as with the Perdew–Burke–Ernzerhof (PBE)[60] parametrization, including dispersion correction from Grimme (D3)[61] to take into account vdW interactions. A dense Monkhorst–Pack grid of *k*-special points was used to perform Brillouin zone (BZ) integrations to ensure high convergence of 1–2 meV per atom in the total energy. Calculating the forces on atoms and the stress tensor, the atomic positions, and the unit cell parameters were fully optimized to obtain the relaxed structures at selected volumes. In the relaxed optimized configurations, the resulting forces on the atoms are less than 0.006 eV Å$^{-1}$, with deviations of the stress tensor from hydrostatic conditions (diagonal tensor) lower than 0.1 GPa.

# 5. Results and discussion

## 5.1 Characterization of samples at room pressure

Both samples #1 and #2 were characterized by powder XRD measurements performed at room conditions (Fig. 1) on a Bruker D8 Advance diffractometer in Bragg–Brentano configuration by using Cu K$_{\alpha 1}$ radiation. Rietveld refinement of sample #1 at RP identified β-As$_2$Te$_3$ as well as a small amount of the initial α-As$_2$Te$_3$ phase used for the synthesis of β-As$_2$Te$_3$. In addition, we found two peaks that most probably also correspond to elemental Te (see asterisks in Fig. 1). On the other hand, Le Bail analysis of sample #2 at RP also identified β-As$_2$Te$_3$ and a small amount (∼1%) of an impurity, we have attributed it to elemental Te, that seems to be a different impurity from that suggested in ref. 14

The lattice parameters and volume of both samples as well as their fractional coordinates, respectively, as obtained from Rietveld refinement are provided in Tables S1 and S2 (ESI‡). Note that owing to the high preferential orientation of the crystallites in sample #2, the position of the atoms in the lattice are not reported in Table S2 (ESI‡). Our experimental and theoretical values for both samples are in good agreement with the experimental values previously reported for β-As$_2$Te$_3$,[8,12,14] what clearly shows that As$_2$Te$_3$ samples grown by the two mentioned methods correspond to β-As$_2$Te$_3$. Note that our sample #2 is the same as the one used in ref. 14; therefore, the lattice parameters and the volume that we have obtained are consistent with those already reported.

Vibrational characterization of both samples of β-As$_2$Te$_3$ *via* RS measurements at ambient conditions is also shown in Fig. 1. The rhombohedral $R\bar{3}m$ structure of β-As$_2$Te$_3$ is centrosymmetric and has a primitive cell with Te1 atom located at a 3a Wyckoff position whereas As and Te2 atoms occupy 6c Wyckoff sites. Consequently, group theory predicts 10 zone-centre modes ($\Gamma_{10} = 2A_{1g} + 3A_{2u} + 2E_g + 3E_u$). The two acoustic branches come from one $A_{2u}$ and a doubly degenerated $E_u$ mode, while the rest correspond to optical modes. Gerade (g) modes are Raman active, while ungerade (u) modes are infrared (IR) active. Therefore, there are four Raman-active modes ($2A_{1g} + 2E_g$) and four IR-active modes ($2A_{2u} + 2E_u$). The E modes correspond to atomic vibrations in the plane of the layers, while the A modes correspond to vibrations along the *c* axis perpendicular to the layers. From now on, we will note the optical vibrational modes with a superscript in order of increasing frequency.

**1040** | *J. Mater. Chem. C*, 2023, **11**, 1037–1055

This journal is © The Royal Society of Chemistry 2023

The RS spectra at ambient pressure of both samples are dominated by a strong broad band between 110 and 150 cm$^{-1}$. Additional bands near 70, 90, and 200 cm$^{-1}$ are also observed. The strong broadband has two or three maxima: one between 120 and 130 cm$^{-1}$, another near 125–135 cm$^{-1}$ and the smallest around 140–145 cm$^{-1}$. Two of these maxima in the broadband have been observed in a previous characterization of the RS spectra of bulk and 2D Te-based chalcogenides at ambient conditions.[62] We will see later that the bands near 90, 120 and 140 cm$^{-1}$ show a negative or a negligible pressure coefficient, as the Raman-active modes of crystalline trigonal Tellurium.[63] Therefore, the strong Raman modes near 120 and 140 cm$^{-1}$ and the weak mode near 90 cm$^{-1}$ in the RS spectrum of β-As$_2$Te$_3$ are identified as the modes of trigonal elemental Te. In particular, they correspond to the breathing mode A$_1$ (120 cm$^{-1}$) and the two doubly degenerate E modes of Te: asymmetric stretching E$^2$ (140 cm$^{-1}$) and rotation E$^1$ (90 cm$^{-1}$), as recently demonstrated.[62] In contrast, we will see later that the bands near 70, 135, and 200 cm$^{-1}$, that have positive pressure coefficients, agree with three (A$_{1g}^1$, E$_g^2$ and A$_{1g}^2$) of the four theoretically predicted Raman-active modes of tetradymite-like As$_2$Te$_3$.[34,35,64] Their experimental and theoretical frequencies and pressure coefficients will be later discussed and summarized in Table 3.

It is quite annoying that the RS spectra of β-As$_2$Te$_3$ are not well observed at room conditions if we consider that the RS spectra of isostructural α-Sb$_2$Te$_3$ and α-Bi$_2$Te$_3$ at room conditions have been very well observed without traces of the RS spectrum of trigonal Te. In order to understand the different RS spectra of β-As$_2$Te$_3$ and those of isostructural α-Sb$_2$Te$_3$ and α-Bi$_2$Te$_3$ at room conditions, we have made a simulation of the unpolarized RS spectra of the three compounds at 0 GPa (Fig. S1, ESI‡). As observed, the RS cross section of some modes of β-As$_2$Te$_3$ is larger than those corresponding to isostructural α-Sb$_2$Te$_3$ and α-Bi$_2$Te$_3$. This means that we should have observed a RS spectrum of β-As$_2$Te$_3$ with some peaks showing a larger intensity than the corresponding ones in isostructural α-Sb$_2$Te$_3$ and α-Bi$_2$Te$_3$; *i.e.* contrary to what is experimentally observed. Therefore, the small intensity of the Raman peaks in β-As$_2$Te$_3$ must be attributed to another cause. For this reason, we have performed *ab initio* calculations of the enthalpy difference, ΔH, at 0 GPa between the above compounds and that of the sum of the elements constituting those compounds; *i.e.* As + Te, Sb + Te, Bi + Te (see Fig. 2(a)). Surprisingly, ΔH between β-As$_2$Te$_3$ and As + Te is only 57 meV; *i.e.* double of the room temperature energy (25 meV); while ΔH between α-Sb$_2$Te$_3$ and α-Bi$_2$Te$_3$ with respect to Sb + Te and Bi + Te is 656 and 1187 meV, respectively. This means that both α-Sb$_2$Te$_3$ and α-Bi$_2$Te$_3$ are very stable compounds, while β-As$_2$Te$_3$ is a rather unstable compound from the energetic point of view. This energetic instability also applies to the other polymorph of As$_2$Te$_3$ (α-As$_2$Te$_3$) with a ΔH around 40 meV. These results for α-As$_2$Te$_3$ and β-As$_2$Te$_3$ suggest that a moderate heating induced by laser excitation during RS measurements at room conditions can lead to the decomposition of the samples of both polymorphs into their constituents. Therefore, these results can explain why Te-related modes are observed in the RS spectrum
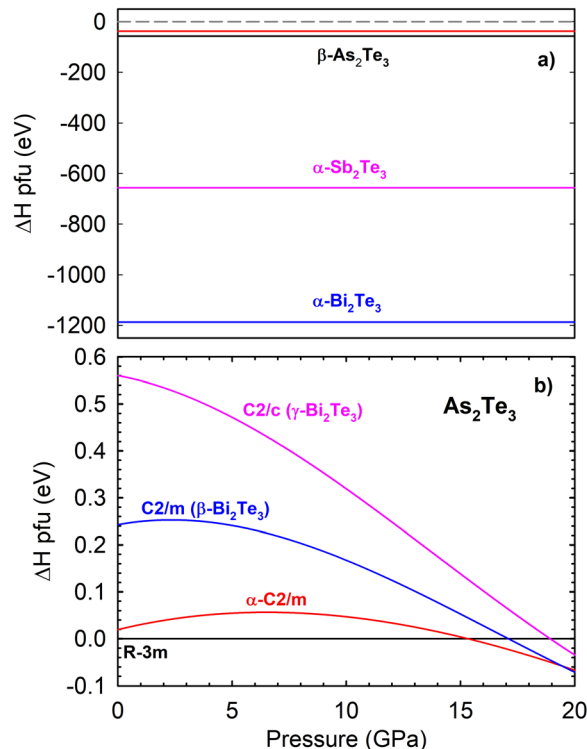


Fig. 2 (a) Theoretical (PBE + D3) enthalpy difference at 0 GPa of the compounds α-As$_2$Te$_3$ (red line), β-As$_2$Te$_3$ (black line), α-Sb$_2$Te$_3$ (blue line), and α-Bi$_2$Te$_3$ (pink line) with respect to their constituents As + Te, Sb + Te, and Bi + Te (gray dashed line). (b) Theoretical (PBE + D3) enthalpy difference (relative to β-As$_2$Te$_3$) *vs.* pressure for the possible crystal structures of As$_2$Te$_3$ upon compression, *i.e.*, α-As$_2$Te$_3$ (C2/m), β-Bi$_2$Te$_3$ (C2/m) and γ-Bi$_2$Te$_3$ (C2/c) structure types.

of both α-As$_2$Te$_3$[21] and β-As$_2$Te$_3$[65] at room conditions. Moreover, we can speculate here that this explanation could be valid to explain why Te-related modes are also observed in a number of other tellurides, as recently commented.[62] In summary, our structural and vibrational characterization of the two studied samples at room conditions shows that, despite the different growth methods, both samples show similar properties and both correspond to β-As$_2$Te$_3$.

### 5.2 HP-XRD measurements

Powder angle-dispersive HP-XRD patterns at selected pressures of sample #1 (up to 17.9 GPa) and sample #2 (up to 18.1 GPa) and down to room pressure, respectively, are shown in Fig. 3. Note that since HP-XRD measurements in the two samples were performed with different X-ray wavelengths, the reflections appear at different 2θ angles; however, the XRD patterns of the β phase as pressure increases are very similar in both samples with all diffraction peaks shifting to higher angles as pressure increases. In addition to the signal of β-As$_2$Te$_3$, sample #1 inside the DAC shows a small amount of α-As$_2$Te$_3$ (see asterisks in Fig. 3(a)), but does not show traces of the impurity associated with elemental Te observed outside the DAC (see Fig. 1). On the other hand, the sample #2 inside the DAC shows traces of elemental Te (see asterisks in Fig. 3(b)).
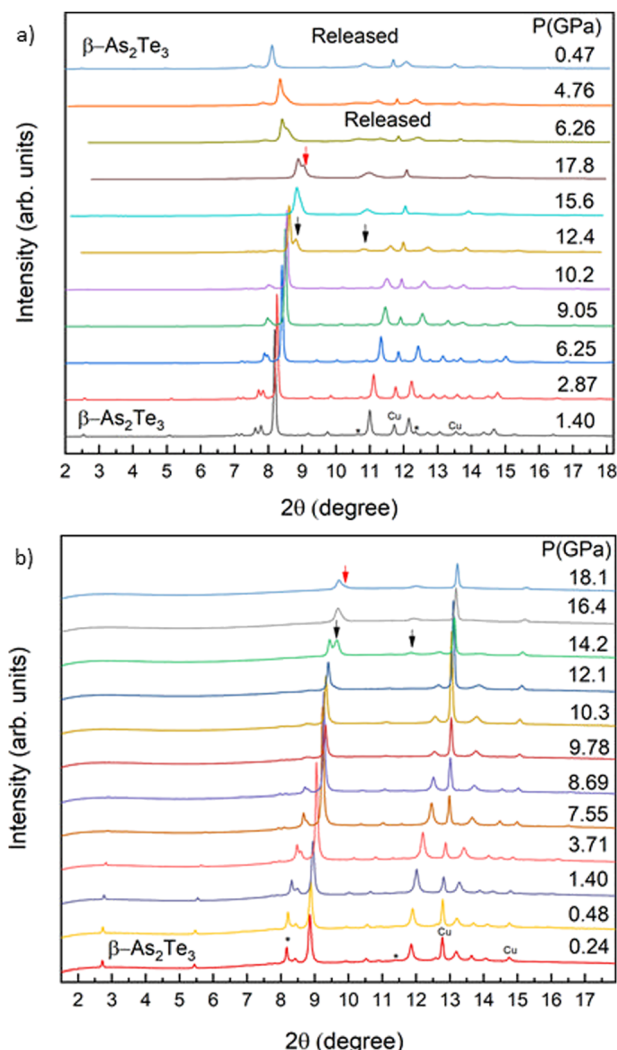
This journal is © The Royal Society of Chemistry 2023

*J. Mater. Chem. C*, 2023, **11**, 1037–1055 | **1041**

Fig. 3 Selected XRD patterns of sample 1 up to 17.9 Gpa (a) and sample 2 up to 18.1 GPa (b). Asterisks in (a) indicate two peaks of the α-As₂Te₃ impurity. Asterisks in (b) indicate the two main peaks of the Te impurity. In fact, the stronger Te impurity peak is a mixture of β-As₂Te₃ and metallic Te peaks. Copper peaks are also indicated. Black and red arrows indicate the positions of new peaks corresponding to high-pressure phases.

Due to the good quality of the XRD patterns and the very small amount of α-As₂Te₃ phase present in sample #1, we performed Rietveld refinements at low pressures without including the α phase (see Fig. S2a of the ESI‡ at 1.75 GPa). Unfortunately, we could only perform Le Bail analysis of the XRD patterns at higher pressures. In sample #2, we performed Rietveld refinements in XRD patterns at all pressures but including elemental Te (see Fig. S2b of the ESI‡ at 1.40 GPa).

As shown in Fig. 3(a) and (b), β-As₂Te₃ undergoes two clear pressure-induced PTs up to 18 GPa. The onset of the 1st PT starts around 9 GPa (Le Bail fits of the experimental data in both samples showed complications to fit the original $R\bar{3}m$ phase above this pressure); however, clear signs of the PT due to the appearance of new peaks occur in the range 12–14 GPa (see black arrows in Fig. 3(a) and (b)). The onset of the 2nd PT is in the range of 18 GPa (see red arrows in Fig. 3(a) and (b)).

To better illustrate the two PTs, we show in Fig. S3 and S4 of the ESI‡ all the diffractograms of the two samples in four sequences covering pressures from 1.42 to 17.9 GPa for sample #1 and from 0.24 to 18.1 for sample #2.

Although it is beyond the scope of this study to determine these two PT, we have calculated the $\Delta H$ curve (relative to β-As₂Te₃) of several possible HP phases of As₂Te₃ (see Fig. 2(b)). They include the α phase (SG $C2/m$) as well as two HP phases of tetradymite α-Sb₂Te₃ and α-Bi₂Te₃: β-Bi₂Te₃ (SG $C2/m$) and γ-Bi₂Te₃ (SG $C2/c$).[66] It can be concluded that α-As₂Te₃ is competitive with β-As₂Te₃ phase from 0 to 15 GPa, β-Bi₂Te₃ is competitive above 17 GPa, and γ-Bi₂Te₃ at much higher pressures.

We emphasize that the PTs of sample #1 are partially reversible after increasing pressure to 17.9 GPa and releasing pressure (see patterns of the recovered sample at the top of Fig. 3(a)). A more detailed picture comparing the upward and downward diffractograms near room pressure (see Fig. S5 of ESI‡) shows that the recovered phase is a disordered β phase, as evidenced by the broadening of the diffraction peaks. This is an interesting result since one could expect that the recovered phase on decreasing pressure from 18 GPa in β-As₂Te₃ would be the stable α phase ($C2/m$) and not the metastable β phase ($R\bar{3}m$) according to enthalpy calculations of ref. 22. Note that a reversible transition was also observed in α-As₂Te₃ up to 17 GPa.[39] Our calculations including dispersion corrections show that the $R\bar{3}m$ phase is thermodynamically more stable than the $C2/m$ phase (Fig. 2(b)). Therefore, the return to the original $R\bar{3}m$ phase in our samples seems to be consistent with the $\Delta H$ plot shown in Fig. 2(b) and with the $R\bar{3}m$–$C2/m$–$C2/c$ sequence of phase transitions observed in Sb₂Te₃ and Bi₂Te₃. Altogether, our enthalpy calculations and those of ref. 22 allow us to conclude that both α and β phases are very competitive in the range between 0 and 15 GPa in As₂Te₃. It is worth commenting that a competitivity of the tetradymite $R\bar{3}m$ phase at room pressure with the supposedly more stable $Pnma$ phase has been recently found in Sb₂Se₃.[67] These results show that it is worth exploring both As₂Te₃ and Sb₂Se₃, since they are sesquichalcogenides in which the $R\bar{3}m$ phase is competitive at room pressure, despite it is not the common phase observed at room pressure, unlike in Sb₂Te₃, Bi₂Te₃, α-and Bi₂Se₃.

Despite this work is mainly focused on the study of the $R\bar{3}m$ phase of As₂Te₃, we show Le Bail analysis of the diffractogram of sample #1 at 15.6 GPa using two $C2/m$ phases (α-As₂Te₃ and β-Bi₂Te₃ in Fig. S7a and b of ESI,‡ respectively), since both phases are candidates for the 1st HP phase of β-As₂Te₃. Both analyses result in relatively good fits but there are also minor peaks that do not fit any of them; therefore, at this moment, no clear conclusion regarding the nature of the 1st HP phase of β-As₂Te₃ can be drawn from the point of view of XRD measurements. Another interesting finding appears when we compare the diffractogram at 17.9 GPa of sample #1 with the one obtained at the same pressure in our previous HP study of α-As₂Te₃ using the same X-ray wavelength (see Fig. S6 of ESI‡).[21] Both diffractograms are very similar, thus confirming that the same HP phase is reached around 18 GPa regardless of the

1042 | J. Mater. Chem. C, 2023, 11, 1037–1055

This journal is © The Royal Society of Chemistry 2023

starting phase (α-As$_2$Te$_3$ or β-As$_2$Te$_3$). In this context, Zhao *et al.*[22] in their HP study of α-As$_2$Te$_3$ suggested the observation of the γ-Bi$_2$Te$_3$-type (SG *C2/c*) phase above 13.2 GPa and the presence of intermediate α' phase and α'' + γ phases (also with SG *C2/m*) at intermediate pressures. Therefore, the conclusive determination of the 1st and 2nd HP phases of β-As$_2$Te$_3$ awaits for future HP-XRD measurements that, in addition, could provide information on whether the stable phase at room conditions is α-As$_2$Te$_3$, as assumed till now, or β-As$_2$Te$_3$, as suggested by our calculations including dispersion corrections.

Let us now analyse the compression of the tetradymite structure in β-As$_2$Te$_3$. Fig. 4 shows the experimental (samples #1 and #2) and theoretical lattice parameters, *c/a* ratio, and unit-cell volume of β-As$_2$Te$_3$ up to 10 GPa. As observed, the pressure dependence of the different magnitudes in the two samples is very similar, thus providing a definitive proof that the two growth methods of samples #1 and #2 yield the same crystalline structure. A monotonous decrease of the experimental and theoretical unit-cell volume with increasing pressure is observed. The fit of pressure *vs.* experimental and theoretical unit-cell volumes to a 3rd-order Birch–Murnaghan equation of state (BM3-EoS)[68] yields the zero-pressure volume, bulk modulus, and pressure derivative of the bulk modulus summarized in Table 1. As observed, there is a rather good agreement between our experimental and our theoretical bulk

**Table 1** Experimental (Exp.) and theoretical (Th.) PBEsol and PBE + D3 data of BM3-EoS for the unit cell volume of β-As$_2$Te$_3$. Theoretical bulk modulus from PBE data of ref. 27 is also given for comparison

| Pressure range (GPa) | $V_0$ (Å$^3$) | $B_0$ (GPa) | $B_0'$ | |
|---|---|---|---|---|
| 0–9 | 415.9(5) | 37(1) | 6.6(4) | Exp. |
| 0–9 | 418.4(2) | 40.1(4) | 6.2(3) | Th. PBE + D3 |
| 0–9 | 405.0(1) | 48.5(5) | 5.9(1) | Th. PBEsol |
| | | 53.2 | | Th. PBE |

moduli and their pressure derivatives, as well as with the previously reported bulk modulus in ref. 27. The experimental bulk modulus is much closer to the value estimated from theoretical PBE + D3 calculations and smaller than the value estimated from theoretical PBE and PBEsol calculations that do not include dispersion corrections to give account for the interlayer interactions. It must be noted that the differences in unit-cell volume compression between the experiment and PBEsol calculations decrease above 3 GPa once interlayer interactions become much stronger than at room pressure. Finally, we must stress that our experimental zero-pressure bulk modulus and its pressure derivative for β-As$_2$Te$_3$ (37 GPa, 6.6) are comparable to the experimental values found in other Te-based tetradymite sesquichalcogenides, like α-Sb$_2$Te$_3$ (36.1 GPa, 6.2)[35,69] and α-Bi$_2$Te$_3$ (35.1 GPa, 6.2).[70] A notable difference in bulk modulus and its pressure derivative is found
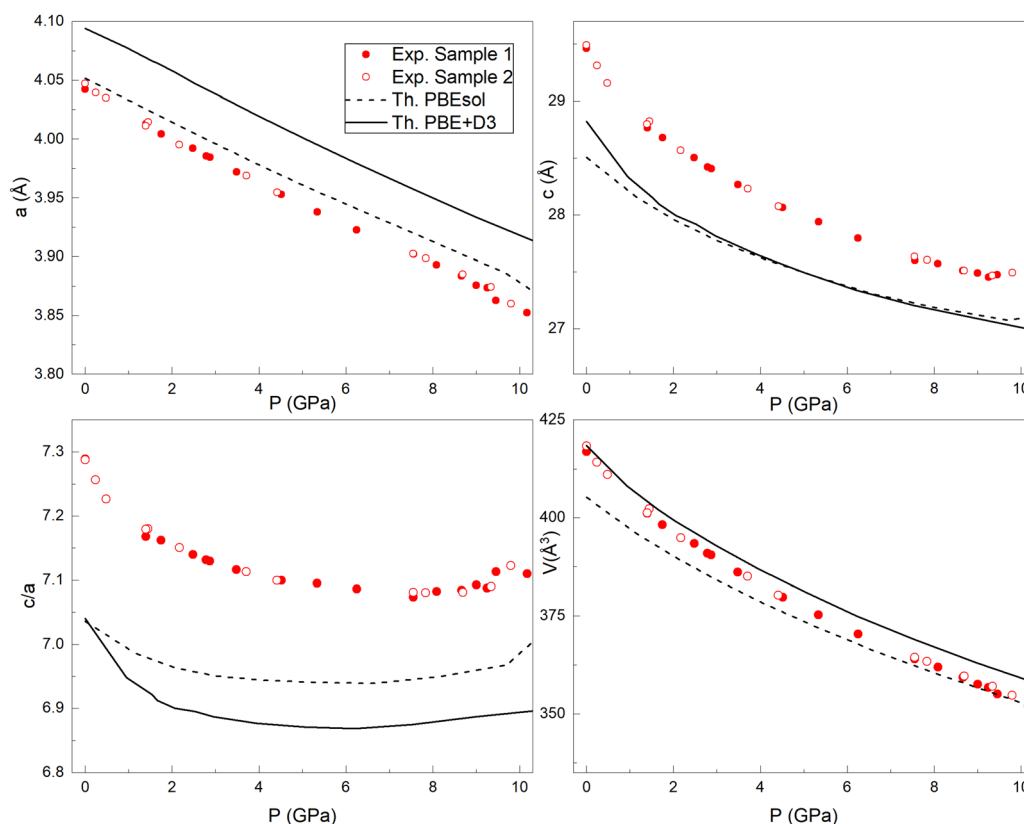


**Fig. 4** Experimental (sample #1 and #2) and theoretical pressure dependence of the lattice parameters, *c/a* ratio, and unit-cell volume of β-As$_2$Te$_3$. Filled and empty circles refer to our experimental results of sample #1 and #2, respectively. Black continuous and dashed lines refer to theoretical PBE + D3 and PBEsol calculations, respectively.

between Te-based sesquichalcogenides and α-Bi$_2$Se$_3$ (53.8 GPa, 2.9).[64]

As regards the lattice parameters, the $a$ lattice parameter decreases almost linearly with pressure, and a good agreement between experimental and theoretical results is obtained, especially for PBEsol data. On the other hand, the experimental $c$ parameter shows a strong non-linear behavior, with a fast-initial decrease up to ca. 2 GPa, due to the strong compression of the interlayer distance at high pressures. This fact is not well described by PBEsol calculations, but very well described by PBE + D3 calculations, which gives a better account of interlayer interactions. As already commented for the unit-cell volume, both experimental and theoretical (PBEsol and PBE + D3) results show a similar compression of the $c$ axis above 3 GPa, due to the strengthening of the interlayer interactions. In relation to the structural $a$ and $c$ parameters, we have observed a strong decrease of the $c/a$ ratio below 2 GPa and a minimum of the $c/a$ ratio around 6.5(1) GPa. The latter will be discussed in relation to the existence of a possible IPT.

Fits of pressure vs. the experimental and theoretical lattice parameters $a$ and $c$ have been performed with a modified BM-EoS, $x(P) = x_0 \left(1 + \dfrac{B_0'}{B_0}P\right)^{-\frac{1}{3B_0'}}$, and the corresponding values of axial zero-pressure bulk moduli and their pressure derivatives are summarized in Table 2. Correspondingly, we have obtained the experimental and theoretical pressure dependence of the $a$ and $c$ axial compressibilities, $k_x = -\dfrac{1}{x}\dfrac{\mathrm{d}x}{\mathrm{d}P}$, with $x = a$ and $c$, as well as that of the bulk modulus, $B = \dfrac{1}{2k_a + k_c}$ (see Fig. 5(a) and (b)). Our results confirm that the experimental $c$-axis compresses much faster than the $a$-axis, especially up to ca. 2 GPa, in good agreement with PBE + D3 calculations, what clearly suggests that the character of the interlayer bonds, assumed to be of vdW type at room pressure, change as pressure increases, especially above 2 GPa. A similar conclusion can be drawn from the pressure dependence of the $c/a$ axial ratio (Fig. 4) and of the axial compressibilities (inset of Fig. 5(a)). In relation to the bulk modulus, we observe that experiments show a monotonous increase with pressure and that the growth rate is more pronounced up to ca. 2 GPa, in good agreement with calculations.

In order to understand the similarities and differences between the compressions of the tetradymite structure in different Te-based sesquichalcogenides, we show in Fig. 5(c) and (d) a comparison of theoretical (PBE + D3) results for β-As$_2$Te$_3$, α-Sb$_2$Te$_3$ and α-Bi$_2$Te$_3$. The three isostructural compounds show similar trends in their axial compressibilities and

bulk modulus with increasing pressure. Surprisingly enough, the axial compressibilities of $a$ and $c$ lattice parameters of β-As$_2$Te$_3$ have smaller values than those of α-Bi$_2$Te$_3$ and α-Sb$_2$Te$_3$, thus resulting in a slightly larger bulk modulus of the former compound (Fig. 5(d) and Table S3, ESI‡). Another difference is that both $k_a$ and $k_c$ values become equal at much larger pressures (∼5.5 GPa) in β-As$_2$Te$_3$ than in α-Bi$_2$Te$_3$ and α-Sb$_2$Te$_3$ (close to 3 GPa) (inset of Fig. 5(c)). Noteworthy, these pressure values are close to those of the IPTs found in different compounds (associated to ETTs in α-Bi$_2$Te$_3$ and α-Sb$_2$Te$_3$).[34,35]

In relation to the bulk moduli (Fig. 5(d)), one would expect a decrease of the bulk modulus with increasing the unit-cell volume of the tetradymite structure on going from As$_2$Te$_3$ to Bi$_2$Te$_3$ according to the inverse relation between volume and bulk modulus. This trend is well observed in our PBE + D3 calculations on going from As$_2$Te$_3$ to Sb$_2$Te$_3$, where both unit-cell volume and bulk moduli show a difference of ∼15%; however, it is not found on going from Sb$_2$Te$_3$ to Bi$_2$Te$_3$ (see Table S3, ESI‡). This result contrasts with experimental results that show a higher value for α-Sb$_2$Te$_3$ (36.1 GPa, 6.2)[35,69] than for α-Bi$_2$Te$_3$ (35.1 GPa, 6.2),[70] that is expected due to the ∼5% difference in unit-cell volumes between both compounds. At present, we are not sure why experimental trends for α-Sb$_2$Te$_3$ and α-Bi$_2$Te$_3$ are not reproduced by PBE + D3 calculations; however, it must be stressed that the obtention of bulk moduli are strongly dependent on the range considered and uncertainties above 5% can be obtained. Therefore, the slightly higher theoretical values of the zero-pressure bulk modulus of α-Bi$_2$Te$_3$ than for α-Sb$_2$Te$_3$ could be a consequence of the range chosen when we make the curve fit. On the other hand, it seems that the higher bulk modulus value of β-As$_2$Te$_3$ at all pressures is a consequence of its smaller $k_c$ value at low pressures and its small $k_a$ value in the whole pressure range. Note that for β-As$_2$Te$_3$, the small $k_c$ value leads to a large $B$ at low pressures, while the small $k_a$ value leads to a large $B$ at pressures above 1.5 GPa; i.e. once the $k_c$ value of β-As$_2$Te$_3$ becomes slightly larger than the $k_c$ of the of α-Sb$_2$Te$_3$ and α-Bi$_2$Te$_3$. These calculations of bulk modulus as a function of pressure will be used below.

Finally, we must mention that structural changes at ca. 2 GPa are further observed in the change of slope of the theoretical free atomic parameters of the tetradymite-like structure of β-As$_2$Te$_3$ (see Fig. 6). Theoretical values at room pressure agree with experimental values at room pressure except for some values of Shu et al.[12] Experimental values at HP are not shown because our HP-XRD powder samples measurements have not allowed us to provide those values.
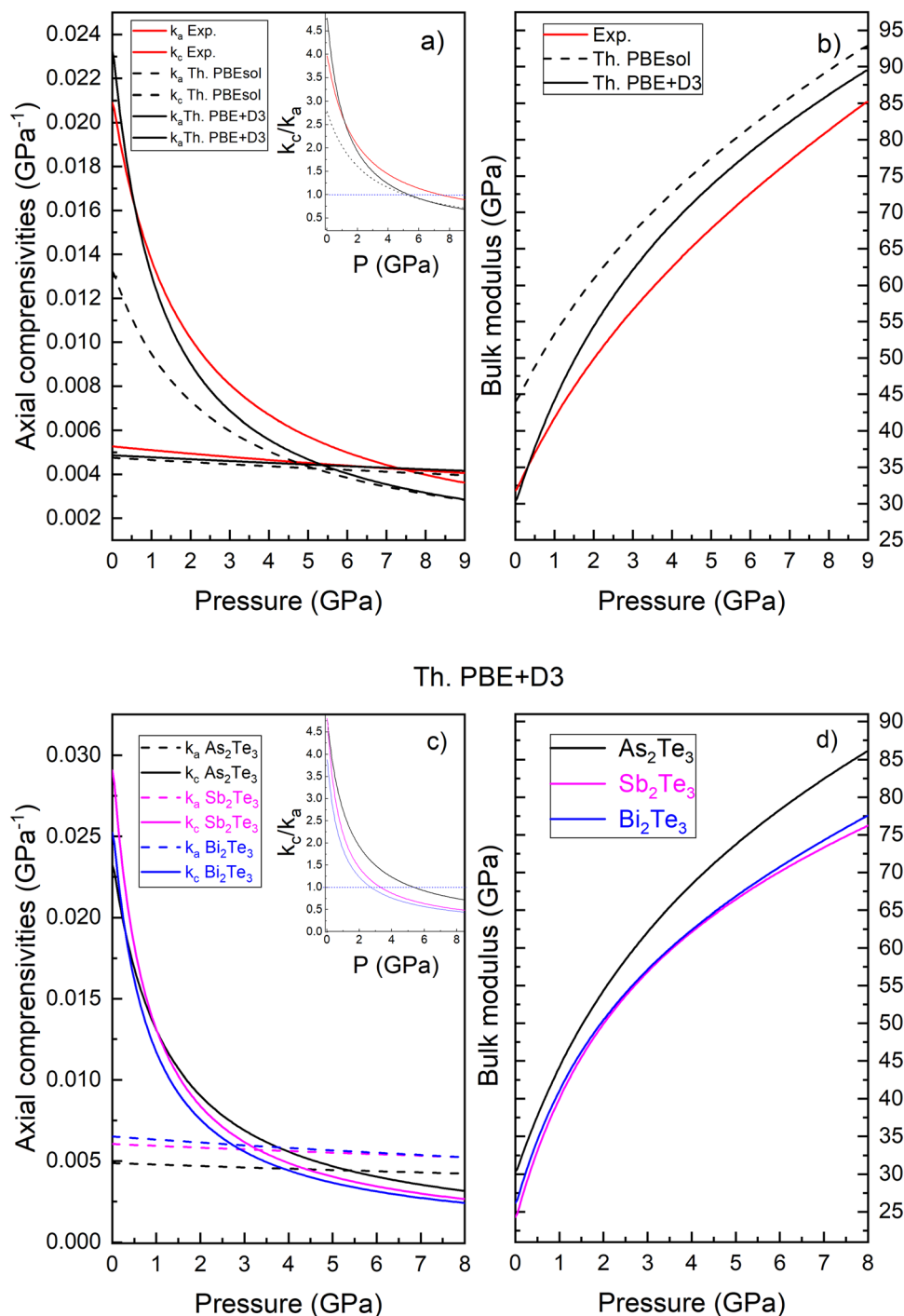
### 5.3 HP-RS measurements

Experimental RS spectra of β-As$_2$Te$_3$ at selected pressures for samples #1 (up to 14.3 GPa) and sample #2 (up to 17.4 GPa), respectively, are shown in Fig. 7(a) and (b). One run (upstroke and downstroke) was done for sample #1 up to 14.3 GPa. Two runs were done for sample #2: run #1 up to 17.4 GPa and run #2 (upstroke and downstroke) up to 7.9 GPa. Only some weak

**Table 2** Experimental (Exp.) and theoretical (Th.) EoS for the lattice parameters of β-As$_2$Te$_3$

|  | $a_0$ (Å) | $B_0$ (GPa) | $B_0'$ | $c_0$ (Å) | $B_0$ (GPa) | $B_0'$ |
|---|---|---|---|---|---|---|
| Exp. | 4.0418(8) | 63(1) | 2.1(3) | 29.45(2) | 15.7(7) | 8.5(3) |
| Th. PBE + D3 | 4.0960(7) | 68(1) | 1.3(3) | 28.810(10) | 14.2(5) | 11.4(2) |
| Th. PBEsol | 4.0516(3) | 70.1(6) | 1.6(1) | 28.508(9) | 24.9(8) | 10.3(3) |

**1044** | J. Mater. Chem. C, 2023, **11**, 1037–1055

This journal is © The Royal Society of Chemistry 2023

**Fig. 5** (color online) Theoretical PBEsol and PBE + D3 (dashed and continuous black line, respectively) and experimental (continuous red line) axial compressibilities (a) and bulk modulus (b) of β-$As_2Te_3$ as pressure increases. Theoretical PBE + D3 comparison of the axial compressibilities (c) and bulk modulus (d) vs. pressure for the three isostructural Te-based sesquichalcogenides (As, Sb, Bi)$_2$Te$_3$ (black, magenta, and blue lines, respectively). Inset of (c) shows the ratio between the compressibilities along the c- and a-axes. The dotted line in the inset represents the pressure at which both compressibilities become equal.

Raman modes of β-$As_2Te_3$ were observed below ca. 2 GPa; however, we clearly observed and followed under pressure the four Raman-active modes of the β phase ($E_g^1$, $A_{1g}^1$, $E_g^2$ and $A_{1g}^2$) above 1.8 GPa in sample #1 and above 2.2 GPa in sample #2, with the $A_{1g}^1$ mode being the most intense one in both samples

up to 9.0 GPa. Above this pressure, in which good fits of XRD data to the tetradymite structure are no longer possible, the $E_g^2$ mode becomes the most intense in both samples. Therefore, HP-XRD and HP-RS measurements indicate that the first HP-PT starts before clear signs on the Raman spectra become evident

This journal is © The Royal Society of Chemistry 2023

J. Mater. Chem. C, 2023, 11, 1037–1055 | 1045
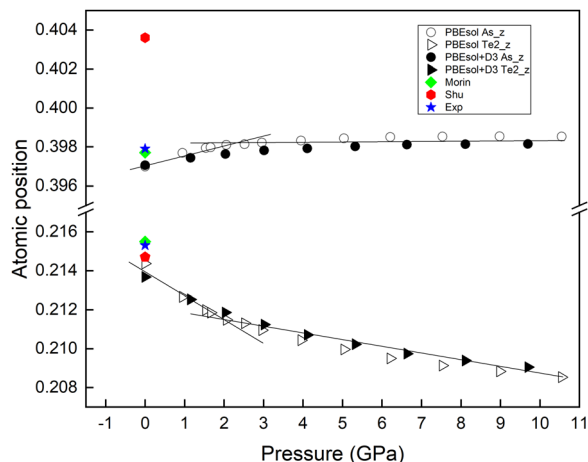
Fig. 6 Theoretical PBEsol and PBE + D3 data (empty and filled triangles, respectively) of the pressure dependence of the free atomic parameters in β-As$_2$Te$_3$. For comparison, we give experimental data at room pressure from this work (blue symbols) and ref. 12 (red symbols) and ref. 14 (green symbols). Straight lines are guides to the eyes to show the change in slope near 2 GPa.

at 12–14 GPa, respectively. The four Raman-active modes of β-As$_2$Te$_3$ could be followed under pressure up to the first-order phase transition above 12 GPa in sample #1 and 14 GPa in sample #2 (the transition in sample #2 seems to be slightly delayed with respect to sample #1).
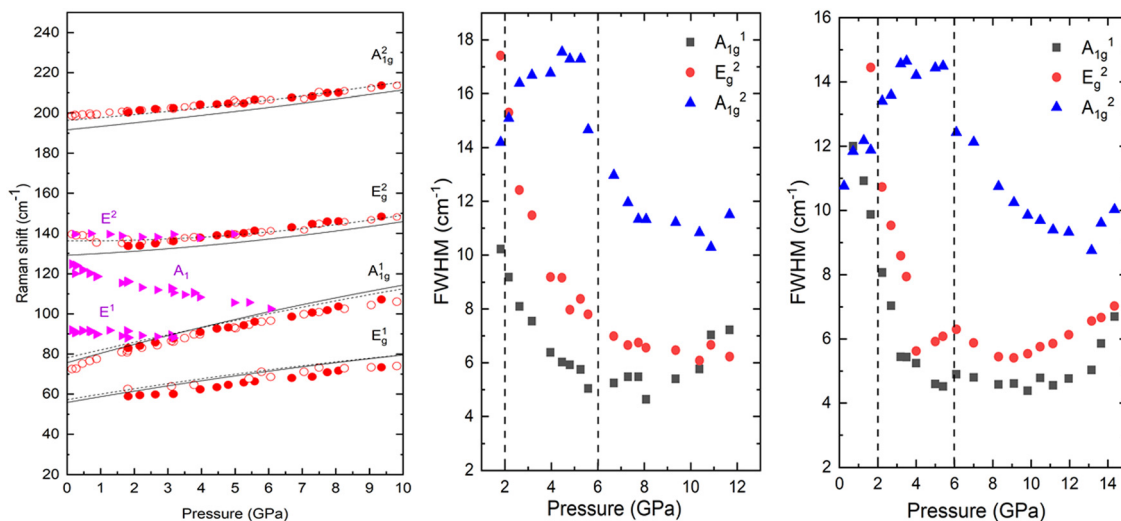
From RP up to about 2.0 GPa, we observed in samples #1 and #2 weak Raman signals of β-As$_2$Te$_3$ and strong Raman modes near 120 and 140 cm$^{-1}$ together with a weak mode near

95 cm$^{-1}$ (see magenta asterisks in Fig. 7(b)). These modes correspond to trigonal elemental Te as mentioned before and their pressure dependence (Fig. 8) is in agreement with a previous work.[63] The situation changes above *ca.* 2 GPa since above this pressure the Raman-active modes of Te are smaller than those of β-As$_2$Te$_3$. We attribute the observation of Te-related modes at low pressures to the decomposition of β-As$_2$Te$_3$ samples into their constituents due to moderate laser-induced heating during RS measurements even at the smallest laser power used since we observed the same RS spectrum in different zones of the samples. In any case, the presence of segregated Te in the original samples inside the DAC cannot be discarded as evidenced by the XRD patterns outside the DAC. Measuring in different zones of sample #1, we were able to follow the four Raman-active modes from 1.8 GPa (see Fig. 7(a)) without elemental Te, since sample #1 has less Te impurities than sample #2, as observed in Fig. 1.

In order to clarify the presence of Te impurity in sample #2, we show a sequence of RS spectra up to 7.6 GPa and their corresponding downstroke obtained during the second run of sample #2 in Fig. S8 of ESI.‡ Apart from the four Raman-active modes of β-As$_2$Te$_3$ (see black arrows in the RS spectrum at 1.8 and 3.4 GPa), we have also followed the pressure dependence of the three Raman-active modes of Te (see magenta asterisks in the RS spectrum at 1.8 GPa). As can be seen, these Te-related Raman modes were observed not only during the upstroke but also in the downstroke even though we checked in different zones of the sample. Therefore, the presence of this impurity is also confirmed by RS measurements. Despite the different Te content in the two samples, we have to stress that
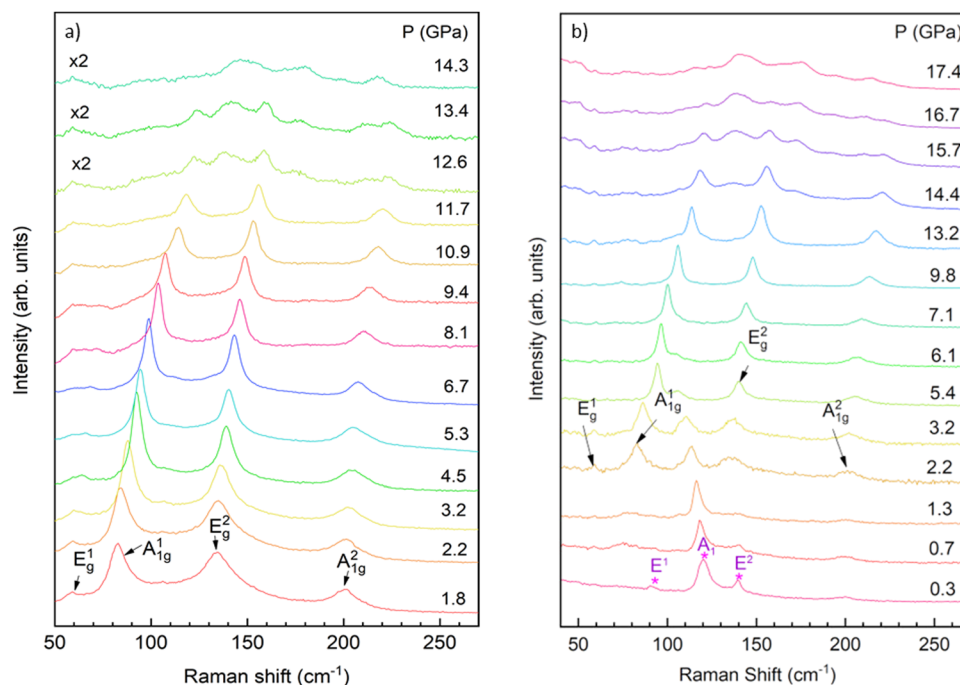


Fig. 7 Experimental Raman spectra of β-As$_2$Te$_3$ at different pressures up to 14.3 GPa for sample #1 (a) and up to 17.4 GPa for sample #2 (b). The four Raman-active modes are indicated with black arrows in both samples and three main modes of the tellurium with asterisks in sample #2.

**1046** | *J. Mater. Chem. C,* 2023, **11**, 1037–1055

This journal is © The Royal Society of Chemistry 2023

**Fig. 8** (left) Experimental (symbols) and theoretical (lines) pressure dependence of the frequencies of the four Raman-active modes of β-As$_2$Te$_3$. Filled and empty circles refer to our experimental results of sample 1 and 2 (run 1 and 2), respectively, and magenta triangles to Te modes in sample 2 (run 1 and 2). Black continuous and dashed lines correspond to theoretical PBE + D3 and PBEsol calculations, respectively. (center) Experimental pressure dependence of the full width at half maximum (FWHM) of some of the Raman-active modes of sample 1 of β-As$_2$Te$_3$. (right) Experimental pressure dependence of the FWHM of some of the Raman-active modes of sample 2 of β-As$_2$Te$_3$. Lines are guides to the eyes. Dashed lines mark the pressure at which the IPTs occur.

we have not been able to measure a clear RS spectrum of β-As$_2$Te$_3$ (with its four Raman-active modes) below 2 GPa, without the presence of intense Te modes from 0 to 2 GPa even outside the DAC, as demonstrated in Fig. 1.

Despite the main focus of the paper is the study of the compression of the tetradymite structure, we want to comment the HP-PTs observed in this compound from the vibrational point of view before analyzing the pressure dependence of the Raman-active modes of β-As$_2$Te$_3$. The RS spectra measured above 12 and 14 GPa in samples #1 and #2, respectively, show broad bands that are compatible with the calculated Raman-active modes of both α-As$_2$Te$_3$ and β-Bi$_2$Te$_3$ since both structures correspond to SG $C/2m$. However, the RS spectra of sample #1 on downstroke from 14.3 GPa (see Fig. S9, ESI‡) show considerable changes below 10 GPa. On one hand, the peaks of the β phase appear; on the other hand, the broad peaks corresponding to the 1st HP phase change. In particular, the single broad band observed below 150 cm$^{-1}$ splits into a double band. Those changes and the instability of the β-Bi$_2$Te$_3$ phase in As$_2$Te$_3$ below 13.3 GPa, according to our lattice dynamics calculations (the lowest B$_g$ mode becomes negative below that pressure), suggest that the broad bands below

10 GPa correspond to α-As$_2$Te$_3$, that is partially recovered on decreasing pressure together with β-As$_2$Te$_3$. Therefore, our RS measurements show that the HP-PTs are only partially reversible (perhaps depending on the hydrostatic conditions or the maximum pressure reached in the experiment). Consequently, our RS measurements confirm the competition of both α and β phases at low pressures. On the other hand, the change of the broad bands around 10 GPa suggest that the 1st HP phase of β-As$_2$Te$_3$ above 12–14 GPa is likely the β-Bi$_2$Te$_3$ phase or a mixture of both α-As$_2$Te$_3$ and β-Bi$_2$Te$_3$. However, this must be confirmed in future experiments.

The experimental and theoretical pressure dependence of the frequencies of the four first-order Raman modes measured in β-As$_2$Te$_3$ is shown in Fig. 8 and the experimental and theoretical first-order Raman mode frequencies and pressure coefficients at room pressure are summarized in Table 3. It can be observed that the frequencies of the four Raman-active modes (red filled circles for sample #1 and red empty circles for sample #2) exhibit a hardening on increasing pressure in good agreement with theoretical calculations. The frequency of the Te modes of sample #2 is indicated by magenta triangles (the A$_1$ mode of Te is easily identified because it has a strong

**Table 3** Theoretical (th.) and experimental (exp.) frequencies at zero pressure ($\omega_0$, in cm$^{-1}$) and pressure coefficients ($a_1$, in cm$^{-1}$ GPa$^{-1}$; $a_2$, in 10$^{-2}$ cm$^{-1}$ GPa$^{-2}$) of β-As$_2$Te$_3$ and Grüneisen parameters at ambient conditions. Frequencies vs. pressure has been fitted to $\omega_0 + a_1P + a_2P^2$

| Mode | β-As$_2$Te$_3$ exp. | | | | β-As$_2$Te$_3$ th. (PBE + D3) | | | |
|---|---|---|---|---|---|---|---|---|
| | $\omega_0$ | $a_1$ | $a_2$ | $\gamma$ | $\omega_0$ | $a_1$ | $a_2$ | $\gamma$ |
| E$_g^1$ | 55(1) | 2.5(3) | −0.05(2) | 1.44813 | 55.8(3) | 2.94(9) | −0.0578(7) | 1.59524 |
| A$_{1g}^1$ | 74(8) | 4.3(3) | −0.08(2) | 1.87457 | 75.7(6) | 4.8(2) | −0.089(1) | 1.90178 |
| E$_g^2$ | 135.5(8) | 0.5(3) | 0.08(2) | 0.11183 | 129(2) | 0.8(6) | 0.08(4) | 0.19813 |
| A$_{1g}^2$ | 198.3(4) | 1.3(2) | 0.03(1) | 0.20889 | 191.6(6) | 1.7(2) | 0.03(1) | 0.26376 |

This journal is © The Royal Society of Chemistry 2023

J. Mater. Chem. C, 2023, **11**, 1037–1055 | **1047**

negative pressure coefficient). The other two Te modes are mixed with two modes of the sample, specifically the $E^1$ with $A_{1g}^1$, and the $E^2$ with $E_g^2$. These latter two modes, which appear between 130 and 140 cm$^{-1}$ are not easily identified since the intensity of Te modes is very high from 0 to 2 GPa. As commented, this is probably caused by the partial decomposition of the sample in that pressure range (see Fig. 1).

It is interesting to compare the experimental pressure coefficients of the four Raman-active modes of β-As$_2$Te$_3$ with those of isostructural Sb$_2$Te$_3$ and Bi$_2$Te$_3$ (see Table S4, ESI‡). Whereas the two low-frequency modes ($E_g^1$ and $A_{1g}^1$) show similar frequency pressure coefficients in the three isostructural compounds (around 2 and 4 cm$^{-1}$/GPa for $E_g^1$ and $A_{1g}^1$, respectively), the two high-frequency modes ($E_g^2$ and $A_{1g}^2$) show similar values in Sb$_2$Te$_3$ and Bi$_2$Te$_3$ (between 3 and 4 cm$^{-1}$/GPa) and much smaller values in β-As$_2$Te$_3$. We think that the smaller values of the two high-frequency modes in β-As$_2$Te$_3$ are due to the slightly different chemical bonding in this compound with respect to its isostructural compounds that will be later commented.

Finally, we want to comment on the changes shown by the intensity and linewidth of the most intense first-order Raman-active modes of β-As$_2$Te$_3$ as a function of pressure. As regards the intensity, it is well seen in Fig. 7 and Fig. S8 (ESI‡) that strong changes in the intensity of most modes are observed near 2 GPa. In fact, in most runs, the four Raman-active modes of β-As$_2$Te$_3$ could only be well observed above ca. 2 GPa. This has posed some questions regarding the behavior of the linewidths of the Raman-active modes of β-As$_2$Te$_3$ because little information is found for some modes, such as the $E_g^1$ mode. The analysis of the best RS spectra of samples #1 and #2 are provided in Fig. 7. They show a strong decrease of the linewidth of $A_{1g}^1$ and $E_g^2$ modes between room pressure and ca. 6 GPa and a slightly increasing linewidth of both modes at higher pressures. On the other hand, the linewidth of the $A_{1g}^2$ mode shows an increase between room pressure and 2 GPa, an approximately constant value between 2 and 5–6 GPa, and a strong decrease at higher pressures. It must be stressed that pressure-induced changes in linewidths in low-bandgap materials have been associated in many cases with topological transitions, like the ETTs or Liftshitz transitions,[71,72] associated with changes in the Fermi surface, and the TQPTs, associated to changes between trivial and non-trivial topological phases.[73,74]

### 5.4 Pressure-induced isostructural phase transitions

Let us now turn our attention to the possible existence of IPTs in β-As$_2$Te$_3$. As already commented, *ab initio* calculations have predicted that β-As$_2$Te$_3$ under uniaxial strain in the *c*-direction would entail a transition from a normal insulator towards a TI at ∼1.7 GPa.[28] Recent theoretical QSGW calculations under hydrostatic conditions have also suggested a transition from a normal insulator to a strong TI; *i.e.* a TQPT, at ca. 2.0 GPa and an insulator-metal transition at ca. 6.5(5) GPa.[29] As mentioned before, our XRD experiments and calculations show a strong decrease of the *c* lattice parameter and of the *c*/*a* ratio up to 2.0 GPa and a minimum of the *c*/*a* ratio around 6.5 GPa

(see Fig. 4). In addition, notable changes in the atomic positions are also observed around 2.0 GPa. On the other hand, changes in the intensity of Raman-active modes are noted between 0 and 1.8–2.0 GPa and also changes of the linewidth of the Raman-active modes are observed near 2.0 and 5.5–6.0 GPa. All these changes suggest that there are two IPTs in β-As$_2$Te$_3$ at ca. 2.0(2) and 6.0(5) GPa. The first IPT is associated to the pressure-induced TQPT and it is specific of β-As$_2$Te$_3$, while the second IPT is associated either to an electronic topological transition (ETT) in a similar way to the ETT occurring in isostructural compounds α-Sb$_2$Te$_3$, α-Bi$_2$Se$_3$, and α-Bi$_2$Te$_3$ near the minimum of the *c*/*a* ratio, or to the semiconductor-metal transition associated to the closing of the bandgap predicted for the topological phase.[29] Since the minimum of the *c*/*a* ratio and the closing of the bandgap are correlated, it seems more plusible to attribute this 2nd IPT to the insulator-metal transition.

In order to find indirect signatures and to complement the clues found by our experimental XRD regarding the possible IPTs, we have performed a topological study of the theoretical (PBE + D3) electronic charge density by calculating the Bader charges of each atom and how they behave with increasing pressure in β-As$_2$Te$_3$ (see Fig. 9). It can be observed that changes of slope in most atoms occur near 2.0 GPa; however there is no clear change around 6.0 GPa from the point of view of Bader charges.

Finally, we have analyzed the behavior under pressure of the three octahedral units of the tetradymite structure of β-As$_2$Te$_3$ showed in Fig. 1; *i.e.* the TeAs$_6$ octahedron (associated to the Te1 atom at the center of the QL), the AsTe$_6$ octahedron (associated to the As atom forming two identical irregular octahedra), and the highly distorted octahedron that we call antiprism (associated to the Te2 atom). For that purpose, we have calculated the pressure dependence of the bond angle variance (BAV) and mean quadratic elongation (QE), which are used to characterize the distortion in coordination polyhedral units.[75] They have been obtained with the VESTA software[76] using our theoretical (PBE + D3) data for β-As$_2$Te$_3$, α-Sb$_2$Te$_3$, and α-Bi$_2$Te$_3$ (Fig. S10, ESI‡). In addition, we have plotted the pressure dependence of the coordination number (ECoN) of these three isostructural Te-based compounds. As expected, the distortion of the octahedron associated with the antiprism of Te2 atoms is much greater than the distortion of the other two octahedra. The distortion of the three octahedral units in the three compounds under compression can be well described by both BAV and QE since the evolution of both parameters with pressure is very similar.

One can look in detail the pressure dependence of the theoretical BAV for the XTe$_6$ and TeX$_6$ octahedra in the three isostructural Te-based compounds. A zoom is shown in Fig. 10(a) and (b). A change near 2.0 GPa in β-As$_2$Te$_3$ is found showing clearly a differentiated behavior in its distortion. The same information is obtained from analogous plots of QE *vs.* pressure (not shown). Therefore, we can conclude that structural changes at 2.0 GPa in β-As$_2$Te$_3$ is specific of this compound, and we attribute them to an IPT associated to the theoretically predicted pressure-induced TQPT.[29]

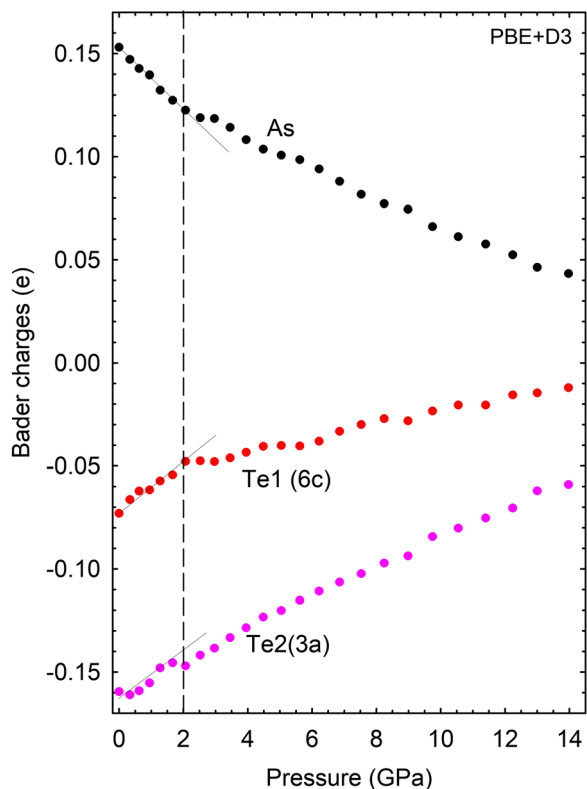**1048** | *J. Mater. Chem. C*, 2023, **11**, 1037–1055

This journal is © The Royal Society of Chemistry 2023

Fig. 9   Pressure dependence of the theoretical (PBE + D3) atomic Bader charges in β-As$_2$Te$_3$.

range of stability of the tetradymite structure in group-15 sesquichalcogenides.

To sum up all observed changes in structural and vibrational properties at *ca.* 2.0(2) GPa can be clearly attributed to an IPT related to the predicted pressure-induced TQPT that transforms β-As$_2$Te$_3$ from a trivial insulator (indeed a low-bandgap semi-conductor) to a 3D Dirac topological semimetal and further to a TI above 2.0 GPa. This behavior appears to be distinct from the other two Te-based compounds that are TIs at ambient conditions. The essential difference comes from the smaller SOC of As atom than of Sb and Bi atoms. The smaller SOC prevents the band inversion of the valence and conduction bands in β-As$_2$Te$_3$, thus resulting in a normal insulator at room pressure. Pressure helps to induce the band inversion because it reduces the bandgap, thus forcing the closing of the bandgap and subsequent reopening once the band inversion occurs at 2.0(2) GPa. At higher pressures, the bandgap of β-As$_2$Te$_3$ reopens and closes again around 6.0(5) GPa,[29] what causes another IPT, that is reflected also in changes in structural and vibrational properties.

### 5.5 Thermoelectric properties

In this section we are going to show that β-As$_2$Te$_3$ can be an excellent thermoelectric material since it has an ultra-low lattice thermal conductivity[29] that is even smaller than that of current industrial thermoelectrics based on α-Bi$_2$Se$_3$, α-Sb$_2$Te$_3$, and α-Bi$_2$Te$_3$.[1,4] For that purpose, we are going to calculate first the strength of the lattice anharmonicity in β-As$_2$Te$_3$. This can be estimated from the mode Grüneisen parameters, $\gamma_i = -\dfrac{d \ln(\omega_i)}{d \ln(V)}$, that characterize the relationship between each phonon frequency, $\omega_i$, and the crystal volume, $V$. From this perspective, the analysis of the phonon anharmonicities could be crucial to reveal the thermal transport properties in thermo-electric materials.[39,78,79] In other words, when the restoring force acting on an atom displaced from its equilibrium position is non-linear, there is a non-zero value of the Grüneisen parameters, $\gamma_i$, that implies a strong influence on the

Interestingly, a minimum occurs in the BAV and QE of the octahedron of the antiprism (Fig. S10, ESI‡) at approximately 12.0, 7.5, and 10.0 GPa for β-As$_2$Te$_3$, α-Sb$_2$Te$_3$, and α-Bi$_2$Te$_3$, respectively. The value of 12.0 GPa is close to the value of instability of the $R\bar{3}m$ phase (above 10 GPa) in β-As$_2$Te$_3$, and the other values are also close to the pressures at which the 1st PT occurs in α-Sb$_2$Te$_3$ and α-Bi$_2$Te$_3$.[22,66,77] In fact, the change at the above mentioned pressures can be clearly seen when plotting the BAV *vs.* QE (Fig. S11, ESI‡). Therefore, we conclude that the behavior of the antiprism at HP allows us to predict the
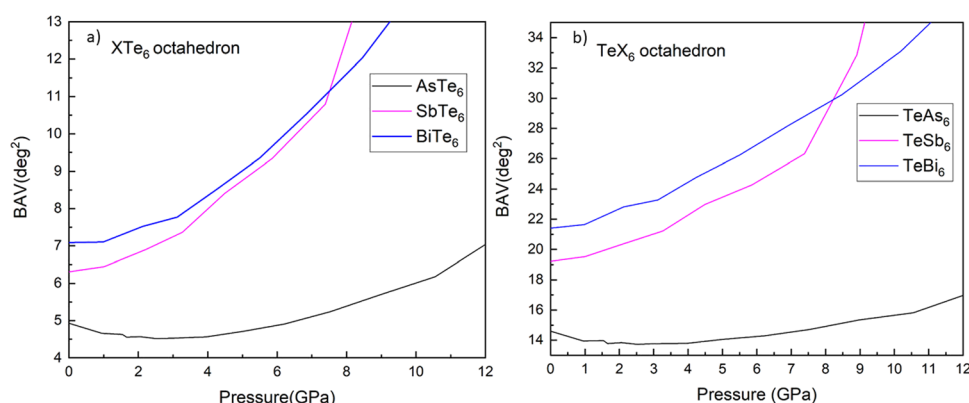


Fig. 10   Theoretical (PBE + D3) pressure dependence of the bond angle variance (BAV) of (a) XTe$_6$ and (b) TeX$_6$ octahedra for β-As$_2$Te$_3$, α-Sb$_2$Te$_3$ and α-Bi$_2$Te$_3$ in black, magenta, and blue colors, respectively.

probability that a frequency phonon interacts with other phonons since anharmonic phonons scatter from each other much more frequently than harmonic phonons. When they scatter, phonons take their momentum and entropy in a different direction from the original one, so the thermal conductivity decreases. Theoretical calculations usually emphasize the significance of acoustic phonons acting in thermal conductivity, but the contributions of optical phonons are always assumed to be negligible due to their relatively low group velocities and large lifetimes.[80,81]

It must be considered, however, that optical phonons are not always negligible, even in simple crystalline bulk materials.[78,82] Taking this into account, we have obtained the experimental and theoretical Grüneisen parameters for each Raman mode as a function of pressure by combining our HP-XRD and HP-RS measurements as well as *ab initio* calculations. For this purpose, we have used the formula $\gamma_i(P) = \frac{B(P)}{\omega_i}\frac{d\omega_i(P)}{dP}$, using the pressure dependence of the bulk modulus reported in Fig. 6(a) and the pressure dependence of the frequency of each phonon fitted to a quadratic function, $\omega_i(P) = \omega_{oi} + a_{1i}P + a_{2i}P^2$, where $\omega_{oi}$ is the phonon frequency at ambient conditions and the fitted values of $a_{1i}$ and $a_{2i}$ are provided in Table 3. The theoretical and experimental values of each mode Grüneisen parameter at room conditions are also provided in Table 3. Fig. 11(a) shows the evolution of the individual Grüneisen parameters, $\gamma_i$, of each Raman mode as pressure increases. As can be seen, the two low-frequency optical Raman modes, $E_g^1$ and $A_{1g}^1$, have Grüneisen values larger than 1.5 in the whole studied pressure range, thus these two low-frequency modes show a considerably anharmonicity

(values above 1) and contribute significantly to the anharmonicity of β-As$_2$Te$_3$.

To understand the anharmonic behavior of β-As$_2$Te$_3$ in relation to its isostructural sesquichalcogenides, we have compared the theoretical mode and average Grüneisen parameters of β-As$_2$Te$_3$, α-Sb$_2$Te$_3$, and α-Bi$_2$Te$_3$ as function of pressure (Fig. 11(b)). Interestingly, all three Te-based isostructural sesquichalcogenides show a highly anharmonic behavior of the two low-frequency optical modes. These results indicate that β-As$_2$Te$_3$ shows a similar anharmonic behavior to α-Sb$_2$Te$_3$ and α-Bi$_2$Te$_3$, two well-known excellent thermoelectric materials. Therefore, our present results confirm previous theoretical calculations that attributed the extremely low lattice thermal conductivity value at room conditions of β-As$_2$Te$_3$ (0.8 W m$^{-1}$ K$^{-1}$) to the low-frequency optical modes that limit the energy window of the acoustic branches.[83]

Let us now turn to the possible good thermoelectric character of β-As$_2$Te$_3$. Semiconductors based on heavy p-block elements (such as Bi, Sb, Se, and Te) that crystallize in the rhombohedral tetradymite structure have long been of interest as the world's best thermoelectrics for room temperature operation and have been continuously studied and developed for that application. We have characterized structurally and dynamically the β-As$_2$Te$_3$ polymorph and compared it with isostructural Te-based chalcogenides (Sb,Bi)$_2$Te$_3$ that have much heavier cations. In general, the efficiency of a thermoelectric system is characterized using the so-called figure of merit, $ZT$, defined as $ZT = \sigma S^2 T / (\kappa_{ele} + \kappa_{lat})$, with $S$, $T$, and $\sigma$ being the Seebeck coefficient, temperature, and electric conductivity, respectively, while $\kappa_{ele}$ and $\kappa_{lat}$ are the electronic and lattice thermal conductivities, respectively.
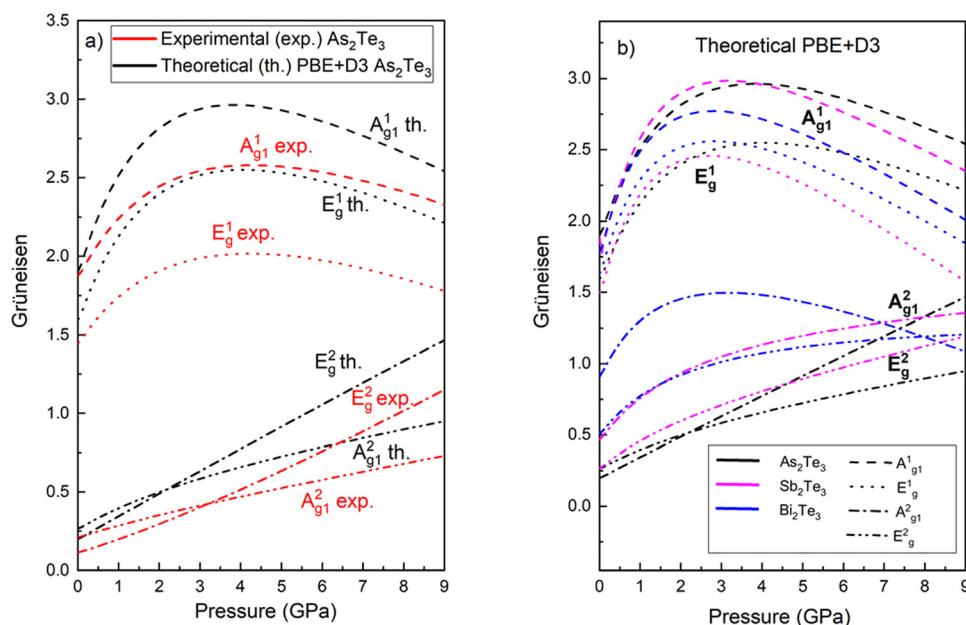


Fig. 11 (a) Pressure dependence of experimental (red colour) and theoretical (PBE + D3) (black colour) of Grüneisen parameters of $E_g^1$, $A_{1g}^1$, $E_g^2$, and $A_{1g}^2$ Raman modes (dot, dash, dash–dot, and dash–dot–dot, respectively) of β-As$_2$Te$_3$. (b) Comparison of the pressure dependence of theoretical (PBE + D3) Grüneisen parameters of the of $E_g^1$, $A_{1g}^1$, $E_g^2$, and $A_{1g}^2$ Raman modes (dot, dash, dash–dot, and dash–dot–dot lines), respectively of the β-As$_2$Te$_3$ (black colour), α-Sb$_2$Te$_3$ (magenta colour), and α-Bi$_2$Te$_3$ (blue colour), respectively.

**1050** | *J. Mater. Chem. C*, 2023, **11**, 1037–1055

This journal is © The Royal Society of Chemistry 2023

In an ideal thermoelectric material, not only a large value of $S$ and $\sigma$ is needed, but also a low thermal conductivity ($\kappa_{ele} + \kappa_{lat}$). Low values of $\kappa_{ele}$ are typical of semiconductors and increase with the doping needed to get a relatively high σ value; however, $\kappa_{lat}$ is a key quantity to reduce $ZT$, since it is an intrinsic property of the material. Therefore, highly efficient thermoelectric semiconductors, in general, have low thermal conductivities.[84–86] $\alpha$-$Bi_2Te_3$ is the working material for most Peltier cooling devices and thermoelectric generators because its alloys with $\alpha$-$Sb_2Te_3$ for p-type and $\alpha$-$Bi_2Se_3$ for n-type material exhibit the highest thermoelectric figure of merit, $ZT$, of any material around room temperature. The exceptional thermoelectric performance of $\alpha$-$Bi_2Te_3$ near room temperature is due to its complex electronic structure and relatively low thermal conductivity.[3,4] Therefore, taking into account that the ultra-low lattice thermal conductivity predicted for $\beta$-$As_2Te_3$[29] is smaller than those reported for $\alpha$-$Sb_2Te_3$ and $\alpha$-$Bi_2Te_3$,[1,4] we can conclude that $\beta$-$As_2Te_3$ can be a very efficient thermoelectric material and its alloys with $\alpha$-$Sb_2Te_3$ and $\alpha$-$Bi_2Te_3$ deserve to be explored.

Moreover, it has been shown that the lattice thermal conductivity of $\beta$-$As_2Te_3$ at room pressure (when $\beta$-$As_2Te_3$ is a trivial insulator) is smaller than at HP (when it is a TI as its iso-structural sesquichalcogenides).[29] Consequently, the smaller lattice thermal conductivity of $\beta$-$As_2Te_3$ at room pressure could open a way to improve the thermoelectric properties of this family of compounds. In this context, it was commented that the ultra-low lattice thermal conductivity of $\beta$-$As_2Te_3$ at room pressure can be due to its proximity to a Kohn anomaly, associated to the occurrence of the 3D TQPT near 2 GPa. In turn, this proximity to the Kohn anomaly is due to the chemical bonding of $\beta$-$As_2Te_3$ since the smaller SOC in this compound prevents the band inversion of the electronic band structure at room pressure. Therefore, As-doped $Sb_2Te_3$ and $Bi_2Te_3$ could be very interesting systems to study since the substitution of Sb and Bi by As would reduce the SOC in these two compounds and will result in a decrease of the bandgap and an approach to the Kohn anomaly associated to the 3D Dirac semimetal phase that occurs prior to the TI phase. This approach to the Kohn anomaly could in turn lead to a reduction of the lattice thermal conductivity in these systems and potentially to an increase of $ZT$.

To this respect, we must recall that the good thermoelectric properties of tetradymites have been recently ascribed to the existence of an unconventional type of bonding.[36–43,45–48,87] This bonding has been named resonant bonding, metavalent bonding, and also hypervalent bonding, but it has been suggested to be named electron-rich multicenter bonding according to a recent review of chemical bonds.[49] The multi-center bond is not as common in solids as in molecules and is characterized by being a hybrid between a covalent or ionic bond, with fully localized electrons, and a metallic bond, with fully delocalized electrons. In chalcogenides, the multicenter bond, with a mix of localized and delocalized electrons, is a weaker bond than the covalent bond and results in a highly polarizable and anharmonic lattice with large Born effective

charges, low bandgaps, large dielectric constants, and very low optical phonon frequencies. In fact, it has been shown that a softening of many high-frequency optical phonons under pressure is observed upon going from a covalent solid, such as $As_2S_3$ at room pressure, to a multicenter solid, such as $As_2S_3$ above 25 GPa.[88] Noteworthy, all phonon frequencies show positive pressure coefficients once multicenter bonding is fully established, but soft phonons show an almost negligible pressure coefficient just before undergoing the transition from a covalent to a multicenter solid.[21,88] Therefore, we think that the small pressure coefficients of the high-frequency modes of $\beta$-$As_2Te_3$ at low pressures, especially the $E_g^2$ mode, together with the positive pressure coefficients found above 2 GPa, indicate that the chemical bonds in $\beta$-$As_2Te_3$ at room pressure do not have a well-developed multicenter bonding character and that such character, typical of $\alpha$-$Sb_2Te_3$, $\alpha$-$Bi_2Te_3$, and $\alpha$-$Bi_2Se_3$, showing phonon modes with positive pressure coeffi-cients,[34,35,64] is reached in $\beta$-$As_2Te_3$ above 2 GPa; i.e. just after the pressure-induced TQPT. This is an interesting result because it points to a link between the multicenter bonding character of tetradymites and its topological properties; a link that has been recently suggested and that could be worthy to explore further.[50]

The presence of an unconventional type of bond in tetra-dymites has been previously suggested because the forces in the interlayer space of tetradymites do not show a typical vdW character, as in transition metal dichalcogenides, since the interlayer space in tetradymites is much smaller than expected in vdW materials.[38,40,67,89] This has been attributed to the presence of the extra delocalized electrons between the layers that contribute an electrostatic component to the bonding that is not present in pure van der Waals materials.[38,40] The extra interlayer electronic charge has been attributed to the presence of multicenter bonding inside the layers. In fact, theoretical calculations of the tetradymite structure in all group-15 sesqui-chalcogenides has shown that they can be arranged in a diagram and that all stable tetradymite sesquichalcogenides are located in a small region of the diagram.[67,89] The multi-center bonding character of some bonds in $\beta$-$As_2Te_3$ was already noted by Yu et al.,[39] who also justified the large anharmonicity of this unconventional bond. Further support for the presence of multicenter bonding in $\beta$-$As_2Te_3$ already at low pressure is shown by the large values of the average optical dielectric constant, $\varepsilon_\infty$, and Born effective charges of $\beta$-$As_2Te_3$ when compared to those of $\alpha$-$As_2Te_3$ (Fig. S12, ESI‡). Note that the average optical dielectric constant of $\beta$-$As_2Te_3$ is almost six times larger than that of $\alpha$-$As_2Te_3$, which shows normal cova-lent bonds. Also the Born effective charges of $\beta$-$As_2Te_3$ are more than almost six times larger than that of $\alpha$-$As_2Te_3$. Finally, it must be stressed that the mixture of covalent and multicenter bondings in this family of materials seems to be related to the different pressure dependence of the (As,Sb,Bi)–Te1 and (As,Sb,Bi)–Te2 bond distances inside the QL (Fig. S13, ESI‡). The covalent (As,Sb,Bi)–Te2 bond distance increases with increasing pressure, while the multicenter (As,Sb,Bi)–Te1 bond distance decreases with increasing pressure. An increase of a

This journal is © The Royal Society of Chemistry 2023

J. Mater. Chem. C, 2023, 11, 1037–1055 | 1051

covalent distance with increasing pressure is not a common feature in solids that has been already observed below 20 GPa in $As_2S_3$ as it undergoes from covalent bonding to multicenter bonding.[88] Note also the different behavior of the Te2–Te2 interlayer distance in $\beta$-$As_2Te_3$ with respect to the other two isostructural compounds and how the interlayer distance in $\beta$-$As_2Te_3$ behaves as in the other compounds above 2 GPa.

In summary, we have found that $\beta$-$As_2Te_3$ shows a strong anharmonic behavior that is consistent with the predicted ultra-low lattice thermal conductivity.[29] These theoretical results are consistent with the good thermoelectric performance of $\beta$-$As_2Te_3$ upon Sn and Bi doping,[15–18] which are better than those of the $\alpha$ phase,[19] and also consistent with the unconventional type of bonding present in group-15 sesqui-oxides with tetradymite structure. Therefore, we hope that studies of alloying $Bi_2Te_3$, $Sb_2Te_3$, and $Bi_2Se_3$ with $\beta$-$As_2Te_3$, that have been barely explored,[10] could be highly rewarding.

## 6. Conclusions

We have performed a joint experimental and theoretical HP structural and vibrational study of $\beta$-$As_2Te_3$. This polymorph of $As_2Te_3$ with tetradymite structure is very interesting because it is isostructural with $\alpha$-$Bi_2Se_3$, $\alpha$-$Sb_2Te_3$, and $\alpha$-$Bi_2Te_3$, which are TIs at ambient conditions, excellent TE materials near room temperature, and show pressure-induced IPTs. Additionally, it has been predicted that $\beta$-$As_2Te_3$ must have an ultra-low lattice thermal conductivity at room pressure and that it must undergo a pressure-induced TQPT around 2 GPa from a trivial semiconductor to a 3D topological Dirac semimetal with a single Dirac cone at the $\Gamma$ point. Moreover, it has been predicted that this compound is a TI above 2 GPa, whose bandgap increases above that pressure and decreases above 4 GPa leading to a metallization above 6 GPa.[29]

We have studied two $\beta$-$As_2Te_3$ samples grown by different methods. Both samples show the same structure and properties, so both correspond to the same phase. We have provided the pressure dependence of the experimental and theoretical lattice parameters and unit-cell volume of $\beta$-$As_2Te_3$ as well as its zero-pressure axial compressibilities and bulk modulus. They have been compared with isostructural sesquichalcogenides. In addition, we have presented a thorough study of the inter-atomic distances and polyhedral distortions. A strong anisotropic compression is observed with a large decrease of the $c$ lattice parameter up to 2.0 GPa and a minimum of the $c/a$ ratio around 6.5 GPa. We have also provided the pressure dependence of the experimental and theoretical frequencies of the Raman-active modes of $\beta$-$As_2Te_3$ as well as their Grüneissen parameters, and linewidths. Again, changes in intensities and linewidths have been found near 2.0 and 6.0 GPa, respectively. All the changes in structural and vibrational parameters occurring near 2.0(2) and 6.0(5) GPa in $\beta$-$As_2Te_3$ suggest the presence of two IPTs that are confirmed by the Bader charge analysis. The two IPTs occur prior to the reversible first-order phase transition above 10 GPa and are of electronic origin; *i.e.* correspond to

phase transitions of order higher than 2, like the pressure-induced IPT and ETT observed in isostructural $\alpha$-$Bi_2Se_3$, $\alpha$-$Sb_2Te_3$, and $\alpha$-$Bi_2Te_3$. Consequently, we conclude that two pressure-induced IPTs are observed in $\beta$-$As_2Te_3$ at 2.0(2) and 6.0(5) GPa. The 1st IPT is related to the pressure-induced TQPT recently proposed to occur near 2 GPa that transforms $\beta$-$As_2Te_3$ from a trivial semiconductor to a 3D topological Dirac semimetal,[29] unlike isostructural sesquichalcogenides. The 2nd IPT is coincident with the closing of the bandgap recently proposed to occur around those pressures, so it corresponds to an insulator-metal transition. This IPT is similar to that found in isostructural sesquichalcogenides.

As regards pressure-induced first-order phase transitions, we have also identified by Le Bail analysis the onsets of the 1st PT and 2nd PT around 10 and 17.9 GPa, respectively. The recovery of both $\alpha$-$As_2Te_3$ and $\beta$-$As_2Te_3$ on decreasing pressure from 18 GPa evidences the competitivity between both polymorphs near room conditions; a result that is in good agreement with our enthalpy calculations. Moreover, we have found that the distortion of the antiprism, containing external Te(6c)–Te(6c) bonds along with two neighbor layers in $\beta$-$As_2Te_3$, $\alpha$-$Sb_2Te_3$, and $\alpha$-$Bi_2Te_3$, seems to govern the pressure at which the 1st first-order PT occurs in these three Te-based sesquichalcogenides.

Finally, we have analyzed the anharmonic behavior of phonons in $\beta$-$As_2Te_3$ and compared it with isostructural $\alpha$-$Sb_2Te_3$, and $\alpha$-$Bi_2Te_3$. The highly anharmonic behavior of the three compounds justifies the low values of the lattice thermal conductivity in tetradymites, especially the ultra-low predicted value found in $\beta$-$As_2Te_3$.[29] Moreover, the anharmonic behavior of tetradymites as well as their structural parameters, like the low value of the vdW gap spacing, have been ascribed to the presence of an unconventional type of bonding named electron-rich multicenter bonding. This bonding is also responsible for the high values of the dielectric constant and Born effective charges in tetradymites.

We hope this work will stimulate further studies in group-15 sesquichalcogenides and related materials due to their capital importance for thermoelectric applications, phase change memories, and topological materials for spintronics and quantum computation. In particular, we consider that alloying of $\beta$-$As_2Te_3$ with $\alpha$-$Sb_2Te_3$ and $\alpha$-$Bi_2Te_3$ could lead to better thermoelectrics due to the closeness of these compounds to the Kohn anomaly related to the TQPT.

## Author contributions

R. Vilaplana: conceptualization, investigation (performing the experiments, Raman sample 1 and 2), formal analysis (XRD and Raman), methodology, writing – review & editing. S. Gallego-Parra: investigation (performing the experiments, Raman sample 1), formal analysis. E. Lora da Silva: software (*ab initio* calculation). D. Martínez-García: resources (grow the sample1 with Paris – Edinburgh cell). G. Delaizir: resources (provide the sample 2). A. Muñoz: software (*ab initio* calculation). P. Rodríguez-Hernández:

**1052** | *J. Mater. Chem. C*, 2023, **11**, 1037–1055

This journal is © The Royal Society of Chemistry 2023

## Conflicts of interest

There are no conflicts to declare.

## Acknowledgements

## References

1 J. P. Heremans, R. J. Cava and N. Samarth, *Nat. Rev. Mater.*, 2017, **2**, 1–21.

2 W. G. Zeier, A. Zevalkink, Z. M. Gibbs, G. Hautier, M. G. Kanatzidis and G. J. Snyder, *Angew. Chem., Int. Ed.*, 2016, **55**, 6826–6841.

3 S. Lee, K. Esfarjani, T. Luo, J. Zhou, Z. Tian and G. Chen, *Nat. Commun.*, 2014, **5**, 1–8.

4 I. T. Witting, T. C. Chasapis, F. Ricci, M. Peters, N. A. Heinz, G. Hautier and G. J. Snyder, *Adv. Electron. Mater.*, 2019, **5**, 1800904.

5 D. Hsieh, Y. Xia, D. Qian, L. Wray, J. Dil, F. Meier, J. Osterwalder, L. Patthey, J. Checkelsky and N. P. Ong, *Nature*, 2009, **460**, 1101–1105.

6 H. Zhang, C.-X. Liu, X.-L. Qi, X. Dai, Z. Fang and S.-C. Zhang, *Nat. Phys.*, 2009, **5**, 438–442.

7 Y. Xia, D. Qian, D. Hsieh, L. Wray, A. Pal, H. Lin, A. Bansil, D. Grauer, Y. S. Hor and R. J. Cava, *Nat. Phys.*, 2009, **5**, 398–402.

8 H. W. Shu, S. Jaulmes and J. Flahaut, *Mater. Res. Bull.*, 1986, **21**, 1509–1514.

9 G. Carron, *Acta Crystallogr.*, 1963, **16**, 338–343.

10 D. Bachan, A. Hovorková, Č. Drašar, A. Krejčová, L. Beneš, J. Horák and P. Lošťák, *J. Phys. Chem. Solids*, 2007, **68**, 1079–1082.

11 V. Kirkinskij and V. Yakushev, *Izv. Akad. Nauk SSSR, Neorg. Mater.*, 1974, **10**, 1431–1435.

12 H. W. Shu, S. Jaulmes and J. Flahaut, *J. Solid State Chem.*, 1988, **74**, 277–286.

13 S. Toscani, J. Dugué, R. Ollitrault and R. Céolin, *Thermochim. Acta*, 1991, **186**, 247–251.

14 C. Morin, S. Corallini, J. Carreaud, J.-B. Vaney, G. Delaizir, J.-C. Crivello, E. B. Lopes, A. Piarristeguy, J. Monnier and C. Candolfi, *Inorg. Chem.*, 2015, **54**, 9936–9947.

15 J. B. Vaney, J. Carreaud, G. Delaizir, A. Pradel, A. Piarristeguy, C. Morin, E. Alleno, J. Monnier, A. P. Gonçalves and C. Candolfi, *Adv. Electron. Mater.*, 2015, **1**, 1400008.

16 J.-B. Vaney, J. Carreaud, G. Delaizir, C. Morin, J. Monnier, E. Alleno, A. Piarristeguy, A. Pradel, A. P. Goncalves and E. B. Lopes, *J. Electron. Mater.*, 2016, **45**, 1786–1791.

17 J.-B. Vaney, G. Delaizir, A. Piarristeguy, J. Monnier, E. Alleno, E. B. Lopes, A. P. Goncalves, A. Pradel, A. Dauscher and C. Candolfi, *APL Mater.*, 2016, **4**, 104901.

18 B. Wiendlocha, J.-B. Vaney, C. Candolfi, A. Dauscher, B. Lenoir and J. Tobola, *Phys. Chem. Chem. Phys.*, 2018, **20**, 12948–12957.

19 J.-B. Vaney, J. Carreaud, G. Delaizir, C. Morin, J. Monnier, E. Alleno, A. Piarristeguy, A. Pradel, A. P. Goncalves and E. B. Lopes, *Adv. Electron. Mater.*, 2016, **45**, 1447–1452.

20 T. Scheidemantel, J. Meng and J. Badding, *J. Phys. Chem. Solids*, 2005, **66**, 1744–1747.

21 V. P. Cuenca-Gotor, J. Sans, J. Ibáñez, C. Popescu, O. Gomis, R. Vilaplana, F. Manjón, A. Leonardo, E. Sagasta and A. Suárez-Alcubilla, *J. Phys. Chem. C*, 2016, **120**, 19340–19352.

22 J. Zhao, L. Yang, Z. Yu, Y. Wang, C. Li, K. Yang, Z. Liu and Y. Wang, *Inorg. Chem.*, 2016, **55**, 3907–3914.

23 Y. Zhang, Y. Ma, A. Geng, C. Zhu, G. Liu, Q. Tao, F. Li, Q. Wang, Y. Li and X. Wang, *J. Alloys Compd.*, 2016, **685**, 551–558.

24 T. Scheidemantel and J. Badding, *Solid State Commun.*, 2003, **127**, 667–670.

25 Y. Sharma and P. Srivastava, *Opt. Mater.*, 2011, **33**, 899–904.

26 L. Debbichi, H. Kim, T. Björkman, O. Eriksson and S. Lebègue, *Phys. Rev. B*, 2016, **93**, 245307.

27 H. Deng, *J. Alloys Compd.*, 2016, **656**, 695–701.

28 K. Pal and U. V. Waghmare, *Appl. Phys. Lett.*, 2014, **105**, 062105.

29 E. L. da Silva, A. Leonardo, T. Yang, M. Santos, R. Vilaplana, S. Gallego-Parra, A. Bergara and F. J. Manjón, *Phys. Rev. B*, 2021, **104**, 024103.

30 N. Sakai and H. Fritzsche, *Phys. Rev. B: Condens. Matter Mater. Phys.*, 1977, **15**, 973.

31 J. Krištofik, J. Mareš and V. Šmíd, *Phys. Status Solidi A*, 1985, **89**, 333–345.

32 K. Ramesh, *J. Phys. Chem. B*, 2014, **118**, 8848–8853.

33 V. Brazhkin, E. Bychkov and O. Tsiok, *Phys. Rev. B*, 2017, **95**, 054205.

34 R. Vilaplana, O. Gomis, F. Manjón, A. Segura, E. Pérez-González, P. Rodríguez-Hernández, A. Muñoz, J. González, V. Marín-Borrás and V. Muñoz-Sanjosé, *Phys. Rev. B: Condens. Matter Mater. Phys.*, 2011, **84**, 104112.

This journal is © The Royal Society of Chemistry 2023

*J. Mater. Chem. C*, 2023, **11**, 1037–1055 | **1053**

35 O. Gomis, R. Vilaplana, F. Manjón, P. Rodríguez-Hernández, E. Pérez-González, A. Muñoz, V. Kucek and C. Drasar, *Phys. Rev. B: Condens. Matter Mater. Phys.*, 2011, **84**, 174305.

36 M. Wuttig, V. L. Deringer, X. Gonze, C. Bichara and J. Y. Raty, *Adv. Mater.*, 2018, **30**, 1803777.

37 J. Y. Raty, M. Schumacher, P. Golub, V. L. Deringer, C. Gatti and M. Wuttig, *Adv. Mater.*, 2019, **31**, 1806280.

38 Y. Cheng, O. Cojocaru-Mirédin, J. Keutgen, Y. Yu, M. Küpers, M. Schumacher, P. Golub, J. Y. Raty, R. Dronskowski and M. Wuttig, *Adv. Mater.*, 2019, **31**, 1904316.

39 Y. Yu, M. Cagnoni, O. Cojocaru-Mirédin and M. Wuttig, *Adv. Funct. Mater.*, 2020, **30**, 1904862.

40 B. J. Kooi and M. Wuttig, *Adv. Mater.*, 2020, **32**, 1908302.

41 Y. Cheng, S. Wahl and M. Wuttig, *Phys. Status Solidi RRL*, 2020, 2000482.

42 L. Guarneri, S. Jakobs, A. von Hoegen, S. Maier, O. Cojocaru-Mirédin, M. Raghuwanshi, M. Drögeler, C. Stampfer, R. Lobo, A. Piarristeguy, A. Pradel and M. Wuttig, *Adv. Mater.*, 2021, **33**, 2102356.

43 J. A. Sans, R. Vilaplana, E. L. da Silva, C. Popescu, V. P. Cuenca-Gotor, A. N. Andrada-Chacón, J. Sánchez-Benitez, O. Gomis, A. L. Pereira and P. Rodríguez-Hernández, *Inorg. Chem.*, 2020, **59**, 9900–9918.

44 T. Kotani, M. van Schilfgaarde and S. V. Faleev, *Phys. Rev. B: Condens. Matter Mater. Phys.*, 2007, **76**, 165106.

45 T. H. Lee and S. R. Elliott, *Phys. Status Solidi RRL*, 2021, **15**, 2000516.

46 T. H. Lee and S. R. Elliott, *Nat. Commun.*, 2022, **13**, 1–12.

47 J. C. Golden, V. Ho and V. Lubchenko, *J. Chem. Phys.*, 2017, **146**, 174502.

48 J. Hempelmann, P. C. Müller, C. Ertural and R. Dronskowski, *Angew. Chem., Int. Ed.*, 2022, **61**, e202115778.

49 R. O. Jones, *J. Phys.: Condens. Matter*, 2022, **34**, 343001.

50 J. F. Khoury and L. M. Schoop, *Trends Chem.*, 2021, **3**, 700–715.

51 F. Fauth, I. Peral, C. Popescu and M. Knapp, *Powder Diffr.*, 2013, **28**, S360–S370.

52 A. Dewaele, P. Loubeyre and M. Mezouar, *Phys. Rev. B: Condens. Matter Mater. Phys.*, 2004, **70**, 094112.

53 C. Prescher and V. B. Prakapenka, *High Press. Res.*, 2015, **35**, 223–230.

54 B. H. Toby, *J. Appl. Crystallogr.*, 2001, **34**, 210–213.

55 W. Kraus and G. Nolze, *Powder Diffr.*, 1998, **13**, 256.

56 H. Mao, J.-A. Xu and P. Bell, *J. Geophys. Res.: Solid Earth*, 1986, **91**, 4673–4676.

57 P. Hohenberg and W. Kohn, *Phys. Rev.*, 1964, **136**, B864.

58 G. Kresse and J. Furthmüller, *Comput. Mater. Sci.*, 1996, **6**, 15–50.

59 J. P. Perdew, A. Ruzsinszky, G. I. Csonka, O. A. Vydrov, G. E. Scuseria, L. A. Constantin, X. Zhou and K. Burke, *Phys. Rev. Lett.*, 2008, **100**, 136406.

60 J. P. Perdew, K. Burke and M. Ernzerhof, *Phys. Rev. Lett.*, 1996, **77**, 3865.

61 S. Grimme, J. Antony, S. Ehrlich and H. Krieg, *J. Chem. Phys.*, 2010, **132**, 154104.

62 F. J. Manjón, S. Gallego-Parra, P. Rodriguez-Hernandez, A. Munoz, C. Drasar, V. Munoz-Sanjose and O. Oeckler, *J. Mater. Chem. C*, 2021, **9**, 6277–6289.

63 C. Marini, D. Chermisi, M. Lavagnini, D. Di Castro, C. Petrillo, L. Degiorgi, S. Scandolo and P. Postorino, *Phys. Rev. B: Condens. Matter Mater. Phys.*, 2012, **86**, 064103.

64 R. Vilaplana, D. Santamaría-Pérez, O. Gomis, F. Manjón, J. González, A. Segura, A. Muñoz, P. Rodríguez-Hernández, E. Pérez-González and V. Marín-Borrás, *Phys. Rev. B: Condens. Matter Mater. Phys.*, 2011, **84**, 184110.

65 J.-B. Vaney, J. Carreaud, A. Piarristeguy, C. Morin, G. Delaizir, R. Viennois, M. Colas, J. Cornette, E. Alleno and J. Monnier, *Inorg. Chem.*, 2018, **57**, 754–767.

66 L. Zhu, H. Wang, Y. Wang, J. Lv, Y. Ma, Q. Cui, Y. Ma and G. Zou, *Phys. Rev. Lett.*, 2011, **106**, 145501.

67 E. L. da Silva, J. Skelton, P. Rodríguez-Hernández, A. Munoz, M. Santos, D. Martínez-García, R. Vilaplana and F. J. J. Manjón, *J. Mater. Chem. C*, 2022, **10**, 15061–15074.

68 F. Birch, *J. Appl. Phys.*, 1938, **9**, 279–288.

69 S. Souza, C. Poffo, D. Triches, J. De Lima, T. Grandi, A. Polian and M. Gauthier, *Phys. B*, 2012, **407**, 3781–3789.

70 A. Polian, M. Gauthier, S. M. Souza, D. M. Trichês, J. C. de Lima and T. A. Grandi, *Phys. Rev. B: Condens. Matter Mater. Phys.*, 2011, **83**, 113106.

71 L. Dagens, *J. Phys. F: Met. Phys.*, 1978, **8**, 2093.

72 F. Manjón, R. Vilaplana, O. Gomis, E. Pérez-González, D. Santamaría-Pérez, V. Marín-Borrás, A. Segura, J. González, P. Rodríguez-Hernández and A. Muñoz, *Phys. Status Solidi B*, 2013, **250**, 669–676.

73 K. Saha, K. Légaré and I. Garate, *Phys. Rev. Lett.*, 2015, **115**, 176405.

74 V. Rajaji, U. Dutta, P. Sreeparvathy, S. C. Sarma, Y. Sorb, B. Joseph, S. Sahoo, S. C. Peter, V. Kanchana and C. Narayana, *Phys. Rev. B*, 2018, **97**, 085107.

75 K. Robinson, G. Gibbs and P. Ribbe, *Science*, 1971, **172**, 567–570.

76 K. Momma and F. Izumi, *J. Appl. Crystallogr.*, 2011, **44**, 1272–1276.

77 J. Zhao, H. Liu, L. Ehm, D. Dong, Z. Chen and G. Gu, *J. Phys.: Condens. Matter*, 2013, **25**, 125602.

78 L.-C. Chen, Q. Peng, H. Yu, H.-J. Pang, B.-B. Jiang, L. Su, X. Shi, L.-D. Chen and X.-J. Chen, *J. Alloys Compd.*, 2019, **798**, 484–492.

79 C. Chang and L.-D. Zhao, *Mater. Today Phys.*, 2018, **4**, 50–57.

80 G. P. Srivastava, *J. Phys. Chem. Solids*, 1980, **41**, 357–368.

81 M. E. Siemens, Q. Li, R. Yang, K. A. Nelson, E. H. Anderson, M. M. Murnane and H. C. Kapteyn, *Nat. Mater.*, 2010, **9**, 26–30.

82 Z. Tian, J. Garg, K. Esfarjani, T. Shiga, J. Shiomi and G. Chen, *Phys. Rev. B: Condens. Matter Mater. Phys.*, 2012, **85**, 184303.

83 J. B. Vaney, J. C. Crivello, C. Morin, G. Delaizir, J. Carreaud, A. Piarristeguy, J. Monnier, E. Alleno, A. Pradel and E. B. Lopes, *RSC Adv.*, 2016, **6**, 52048–52057.

84 L.-D. Zhao, S.-H. Lo, Y. Zhang, H. Sun, G. Tan, C. Uher, C. Wolverton, V. P. Dravid and M. G. J. N. Kanatzidis, *Nature*, 2014, **508**, 373–377.

85  X. Shi, L. Chen and C. Uher, *Int. Mater. Rev.*, 2016, **61**, 379–415.

86  G. J. Snyder and E. S. Toberer, *Materials for sustainable energy: a collection of peer-reviewed research and review articles from Nature Publishing Group*, World Scientific, 2011, pp. 101–110.

87  T. H. Lee and S. R. Elliott, *Adv. Mater.*, 2020, **32**, 2000340.

88  V. P. Cuenca-Gotor, J. Á. Sans, O. Gomis, A. Mujica, S. Radescu, A. Muñoz, P. Rodríguez-Hernández, E. L. da Silva, C. Popescu and J. Ibañez, *Phys. Chem. Chem. Phys.*, 2020, **22**, 3352–3369.

89  R. Wang, F. R. Lange, S. Cecchi, M. Hanke, M. Wuttig and R. Calarco, *Adv. Funct. Mater.*, 2018, **28**, 1705901.

This journal is © The Royal Society of Chemistry 2023

*J. Mater. Chem. C*, 2023, **11**, 1037–1055  |  **1055**